Nuclear blebs are associated with destabilized chromatin packing domains

Emily M. Pujadas Liwag[1,2,3,*], Nicolas Acosta[1,3,*], Luay Matthew Almassalha[1,3,4,*], Yuanzhe (Patrick) Su[1,3], Ruyi Gong[1,3], Masato T. Kanemaki[5,6,7], Andrew D. Stephens[8,9,§] and Vadim Backman[1,3,‡,§]

[1]Department of Biomedical Engineering, Northwestern University, Evanston, IL 60208, USA
[2]IBIS Interdisciplinary Biological Sciences Graduate Program, Northwestern University, Evanston, IL 60208, USA
[3]Center for Physical Genomics and Engineering, Northwestern University, Evanston, IL 60208, USA
[4]Department of Gastroenterology and Hepatology, Northwestern Memorial Hospital, Chicago, IL 60611, USA
[5]Department of Chromosome Science, National Institute of Genetics, ROIS, Mishima, Shizuoka 411-8540, Japan
[6]Graduate Institute for Advanced Studies, SOKENDAI, Mishima, Shizuoka 411-8540, Japan
[7]Department of Biological Science, The University of Tokyo, Tokyo 113-0033, Japan
[8]Biology Department, University of Massachusetts Amherst, Amherst, MA 01003
[9]Molecular and Cellular Biology, University of Massachusetts Amherst, Amherst, MA 01003, USA

[*]co-first authors (contributed equally) and each has the right to place their name first on curriculum vitae
[‡]Lead Contact
[§]Authors for correspondence (Andrew.stephens@umass.edu; v-backman@northwestern.edu)

ABSTRACT

Disrupted nuclear shape is associated with multiple pathological processes including premature aging disorders, cancer-relevant chromosomal rearrangements, and DNA damage. Nuclear blebs (i.e. herniations of the nuclear envelope) have been induced by (1) nuclear compression, (2) nuclear migration (e.g. cancer metastasis), (3) actin contraction, (4) lamin mutation or depletion, and (5) heterochromatin enzyme inhibition. Recent work has shown that chromatin transformation is a hallmark of bleb formation, but the transformation of higher-order structures in blebs is not well understood. As higher-order chromatin has been shown to assemble into nanoscopic packing domains, we investigated if (1) packing domain organization is altered within nuclear blebs and (2) if alteration in packing domain structure contributed to bleb formation. Using Dual-Partial Wave Spectroscopic microscopy, we show that chromatin packing domains within blebs are transformed both by B-type lamin depletion and the

Journal of Experimental Biology • Accepted manuscript

inhibition of heterochromatin enzymes compared to the nuclear body. Pairing these results with single-molecule localization microscopy of constitutive heterochromatin, we show fragmentation of nanoscopic heterochromatin domains within bleb domains. Overall, these findings indicate that chromatin within blebs is associated with a fragmented higher-order chromatin structure.

Keywords: Chromatin Motion, Chromatin Nanodomains, Heterochromatin, Lamins, Nuclear Blebbing

INTRODUCTION

The mammalian cell nucleus is a membrane-enclosed organelle that provides an enclosure chromatin, the assembly of DNA and associated proteins that regulates critical processes such as gene transcription, replication, and DNA repair. Chromatin, chromatin proteins, and chromatin-related processes directly influence nuclear mechanics and shape (Berg et al., 2023; Chiu et al., 2024; Currey et al., 2022; Stephens et al., 2017, 2018). Nuclear stability is further maintained by multiple processes, including by the nuclear lamina, a meshwork of type V intermediate filament proteins called lamins (Funkhouser et al., 2013). Besides its role in maintaining nuclear stiffness and stability, the lamina plays critical roles in regulating gene expression and DNA replication through chromatin interactions. Located immediately underneath the inner nuclear membrane, the lamina consists of four major types of lamin proteins: lamin A, lamin C, lamin B1, and lamin B2. A-type lamins, which consist of lamins A and C, are primarily associated with developmental roles, contribute to nuclear stiffness, mainly expressed in differentiated cells, and are spatially located near the nucleoplasm (Berg et al., 2023; Chiu et al., 2024; Currey et al., 2022; Funkhouser et al., 2013; Nmezi et al., 2019; Stephens et al., 2017, 2018). B-type lamins, in contrast, are expressed in all cell types throughout development and differentiation, provide global integrity of chromatin structure through chromatin-tethering, and are tightly associated with the inner nuclear membrane (Burke and Stewart, 2013; Chang et al., 2022; Nmezi et al., 2019). In mammalian cells, lamins interact with heterochromatin to form lamina-associated domains (LADs), identified through the DamID technique which maps protein-DNA interactions in a genome-wide manner, and are typically transcriptionally repressive environments. Disruption of these LADs has been linked to epigenetic changes in cancer and pre-malignant processes such as the onset and evasion of senescence (Lochs et al., 2019).

Abnormal nuclear morphology and disruption of genome organization are associated with pathologies such as laminopathies (e.g. Hutchinson-Gilford progeria syndrome), cancer, and cardiac disorders (Kalukula et al., 2022; Stephens et al., 2019a, 2018). Among the most radical deformations in nuclear shape is the protrusion of chromatin from the nuclear surface, known as a nuclear bleb, that is associated with pathological transformation (Funkhouser et al., 2013; Karoutas and Akhtar, 2021; Stephens et al., 2019a, 2018). While these blebs are highly associated with gene-rich euchromatin and are believed to only contain lamin A/C, (Nmezi et al., 2019) recent evidence has indicated that non-canonical blebs also contain B-type lamins (Bunner et al., 2024 preprint; Stephens et al., 2018). A- and B-type lamins both contribute to nuclear mechanics and morphology, and depletion of either has been widely shown to induce both abnormal nuclear shape and a higher propensity for nuclear rupture, increased presence of

micronuclei, and more nuclear blebbing events (Kalukula et al., 2022; Karoutas and Akhtar, 2021; Vahabikashi et al., 2022). Nucleus micromanipulation force measurements reveal that the nucleus is softer upon inhibition of either histone deacetylation (HDAC) or histone methyltransferase (HMT) which leads to nuclear bleb formation independent of lamins (Stephens et al., 2019a, 2018). Thus, chromatin and lamins resist external antagonistic forces from actin contraction (Jung-Garcia et al., 2023; Mistriotis et al., 2019; Nmezi et al., 2019; Pho et al., 2024) and compression (Hatch and Hetzer, 2016; Le Berre et al., 2012), as well as internal transcription forces(Berg et al., 2023), to maintain nuclear shape. These studies indicate that nuclear mechanics are influenced by the balance of euchromatin and heterochromatin, and that perturbation of this balance can result in abnormal nuclear morphology and DNA damage, both hallmarks of human disease (Evangelisti et al., 2022; Karoutas and Akhtar, 2021; Stephens et al., 2019a). At the nuclear periphery, the dynamics of cytoskeleton reorganization and chromatin structural changes contribute to mechano-transduction and transcription, independent of lamins. For example, mechanosensitive ion channels embedded in the plasma membrane activate Ca^{2+} signaling upon cellular stress, which can contribute to heterochromatin reorganization and chromatin mobility (Dupouy et al., 2024; Nava et al., 2020; Qin et al., 2021; Stephens et al., 2019a).

Recent work demonstrates that chromatin assembles into higher-order polymeric domain structures (nanodomains, packing domains, chromatin cores), which range between 50-200 nm in size and contain ~200 Kbp to 2 Mbp of genomic content across multiple cell types (Li et al., 2022, 2021; Szabo et al., 2020). A crucial feature of these domains is the formation of high-density centers with surrounding regions of decreased density until a transition into low-density space with RNA-polymerase activity forming primarily at the boundary. In the context of these findings, the structure of the genome assembles from disordered nucleosomes (5 to 25 nm) transitioning into domains (50-150 nm) and then into territorial polymers (>200 nm). As has been previously shown, within the regime of chromatin assembling into domains, chromatin acts as a power-law polymer with dimension, D relating how the mass is distributed within the occupied volume. Notably, within supra-nucleosomal length scales, chromatin is not assembled purely as a space-fulling globule (D=3) nor is it as a poorly structured polymer with monomers primarily favors solvent interactions (D=5/3), instead it is typically within these ranges and varies from cell to cell. A key feature identified in this higher-order assembly is the coupling between heterochromatin centers (dense cores) with euchromatic periphery and a corrugated periphery (Li et al., 2021). As power-law polymeric assemblies, the space filling geometry of these chromatin packing domains is quantifiable by the relationship $M \propto r^D$, relating how genome content fills an occupied volume as a function of its radial distance, r. This organization can be measured by live-cell dual-Partial Wave Spectroscopic (dual-PWS) Microscopy and quantified via the local average chromatin packing scaling $D_a(x,y)$, and its reported ensemble average D_n which is proportional to the volume fraction which these chromatin packing domains occupy within the nucleus and their space filling geometry (Materials and Methods). In addition to quantifying packing domain structure in live cells, PWS microscopy allows measurement of the effective diffusion coefficient, D_e, and the fractional moving mass (FMM) which quantifies the fraction of chromatin demonstrating coherent motion within a diffraction limited volume. Utilizing this technique, we have previously demonstrated that B-type lamin depletion is associated with increased levels of chromatin fractional moving mass and repositioning of heterochromatin cores (Pujadas et al., 2023 preprint; Pujadas Liwag et al., 2024).

A major challenge in studying alteration in chromatin due to blebbing is that these represent infrequent, but critical events in nuclear structure. As such, they are difficult to assess using sequencing-based methods that measure ensemble chromatin organization such as Hi-C or ChIP-Seq and require the utilization of microscopic methods that can directly quantify changes in high-order genome structure. Therefore, in this study, we utilize live-cell PWS microscopy to investigate the interplay between the disruption of the nuclear lamina and heterochromatin enzymes in the structure of higher-order chromatin within blebs. Our results indicate distinct roles for the nuclear lamina and heterochromatin remodeling processes in regulating higher-order chromatin domains both of which are associated with bleb formation. Finally, pairing our findings with super-resolution microscopy, we show that a key transformation of higher-order chromatin within blebs of nanoscopic domains.

RESULTS

B-type lamin depletion or heterochromatin loss promote aberrant nuclear morphology in HCT-116 cells

Bleb formation has been identified in numerous cell types, but the frequencies of bleb formation have been shown to depend on multiple factors. Therefore, we first investigated the role of processes well established to induce bleb formation: inhibition of B-type lamins and disruption in heterochromatin enzymes (Stephens et al., 2018, 2019b). To assess the impact of lamin degradation on nuclear morphology, we applied the AID system to HCT116 colorectal carcinoma epithelial cells to induce simultaneous degradation of lamin B1 and lamin B2 as previously described (Pujadas et al., 2023 preprint; Pujadas Liwag et al., 2024; Yesbolatova et al., 2019). This cell line has an mClover fluorescent reporter fused to the lamin B1/B2 proteins that was used in our degradation experiments. Using immunofluorescence imaging, we quantified the percentages of nuclear blebbing in HCT116$^{LMN(B1\&B2)\text{-}AID}$ cells before and after depletion of B-type lamins by auxin treatment for 24 h. We found that in comparison to untreated controls, auxin treatment promoted a significant increase in the percentage of cells containing nuclear blebs (2.07% vs 6.23%; 4.163±1.033 (Mean difference±s.e.m.), *P*-value=0.016, Student's *t*-test) (Fig. 1A, Table S1), in agreement with past studies (Chen et al., 2018; Stephens et al., 2018; Vargas et al., 2012). Previous work from this group has demonstrated that inhibition of HDACs to increase euchromatin content in mammalian cells or inhibition of histone methyltransferases to decrease heterochromatin content results in a softer nucleus and promotes nuclear blebbing, without perturbing lamins (Stephens et al., 2019a, 2018). We therefore hypothesized that in addition to B-type lamin loss increasing nuclear blebbing, heterochromatin loss would also result in a substantial increase in nuclear blebs in HCT-116 cells. To test this, we treated HCT116$^{LMN(B1\&B2)\text{-}AID}$ cells with either GSK343, an inhibitor of the histone methyltransferase Enhancer of Zeste Homolog 2 (EZH2), or Trichostatin A (TSA), an inhibitor of class I and II HDACs for 24 h.

Our results confirmed that GSK343 and TSA treatment significantly increased the percentage of blebbed nuclei within HCT-116 cells; with TSA treatment also inducing micronuclei formation and associated with a deformed nuclear periphery via increased number of blebs (Fig. 1A, Table S1). The effect of TSA treatment on nuclear blebbing frequency was drastically higher than that of auxin or GSK343 in HCT116$^{LMN(B1\&B2)\text{-}AID}$ cells (Auxin

6.23%, GSK343 6.99%, TSA 15.32%). Next, we explored how combined treatment of either auxin and GSK343 or auxin and TSA would impact the frequency of nuclear blebs. Combination of depletion of B-type lamins with disruption of heterochromatin resulted in only slightly increased rates of nuclear blebs in comparison to lamin depletion, GSK343, or TSA treatment alone (No significant Difference: Auxin+GSK343 7.97%, Auxin+TSA 23.56%) **(**Fig. 1A**).** We found no significant difference between cells treated with or without auxin in both TSA- and GSK343- treated groups (TSA vs TSA+Auxin P=0.078, and GSK343 vs GSK343+Auxin P=0.8235).

Using immunofluorescence microscopy, we visualized these blebs and compared relative levels of H3K27me3 and H3K27ac between the untreated control and auxin, GSK343, and TSA-treated conditions within the cell nucleus (Fig. 1B). Consistent with prior reports, we observe a reduction in H3K27me3 levels upon auxin-induced degradation of B-type lamins and GSK343 treatment respectively. For H3K27ac, we observe an increase in levels in the auxin-treatment group and GSK343 treatment respectively (Fig. 1C,D). Taken together, these results indicated that TSA-mediated heterochromatin disruption promotes nuclear blebbing to similar levels or greater levels than B-type lamin loss in HCT-116 cells.

Nanoscale chromatin packing domains are disrupted within nuclear blebs

We recently demonstrated that the decreased DNA density is conserved across multiple bleb mechanisms and is a consistently preserved feature of blebs (Bunner et al., 2024 preprint). We investigate here in greater detail the influence in the change of higher-order chromatin organization upon bleb formation. While it is commonly assumed that heterochromatin is primarily localized to the nuclear periphery and peri-nucleolar space, recent work with super resolution imaging indicates high-density heterochromatin throughout the nuclear interior. We have previously shown that live-cell PWS microscopy, which does not resolve each individual domain but measures the local ensemble in individual nuclei (Materials and Methods), is sensitive to detecting the assembly into supra-nucleosome structures in individual cells with measurements comparable to those observed on electron microscopy by measuring the variations in the visible-light interference spectrum from within the nucleus (Almassalha Luay et al., 2016; Gladstein et al., 2019, 2018; Li et al., 2022, 2021). The relationship between genomic length (N) and radius (r) can be used to quantify how chromatin is packed within a given volume. This relationship is characterized by the mass fractal dimension (D), which describes how densely the chromatin mass fills the space it occupies. In principle, mass scaling can be quantified at various levels of genome organization: including an entire chromosome or the genomic scaling within individual chromatin packing domains (Li et al., 2022) We focus on supra-nucleosomal domain length-scales (50-150 nm) within this work due to recent observations demonstrating that this regime is paired with crucial functions such as gene transcription (Li et al., 2021; Miron et al., 2020). Partial Wave Spectroscopy (PWS) enables the measurement of local average chromatin packing scaling (D_a) at specific (x,y) locations within the nucleus with sensitivity primarily to structures within the length-scales of chromatin domains (50-200 nm). $D_a(x,y)$ is proportional to the average packing scaling within the coherence volume probed. The nuclear average scaling (D_n), obtained by averaging $D_a(x,y)$ across the nucleus, is proportional to the volume fraction of chromatin domains within the nucleus and their scaling D. As chromatin is organized in mass-fractal packing domains, D_n measures the

likelihood of chromatin organizing into domains with the ensemble scaling. Likewise, we have shown that by analyzing the temporal interference spectrum at a single-wavelength dual-PWS microscopy can measure the temporal evolution of chromatin density and the fractional moving mass (FMM), which measures the volume fraction of- and mass of- chromatin moving coherently with a sensitivity to mass density fluctuations as low as ~5×10−21 g, and the effective diffusion coefficient (De) within the nucleus (ranging between ~0.065 $\mu M^2/s$ to 3.5×10^{-5} $\mu M^2/s$). In the context that the mass of an individual nucleosome $\sim10^{-19}$ g, the typical values of FMM measured represent the movement of nucleosome clutches moving coherently (as an ensemble). With respect to the D_e, the observed values are typically between the observed rate of diffusion for genomic loci ($\sim10^{-4}$ $\mu M^2/s$) and the rate of mRNA through the nucleus ($\sim5\times10^{-2}$ $\mu M^2/s$) (Li et al., 2021). Given these considerations, we utilized dual-live cell PWS microscopy to probe the higher-order structure of chromatin in blebs, nuclei with blebs, and stable nuclei.

Applying dual-PWS to the three well known processes that contribute to bleb formation, we investigated the structure of higher order chromatin and mobility in B-type lamin depletion, HDAC inhibition (TSA), and in EZH2 inhibition (GSK343). As each perturbation has a distinct means to promote bleb formation, we first evaluated the structure of chromatin packing domains observed within blebs in all conditions (controls, EZH2i, HDACi, and lamin depletion) to see if any commonalities were present (Table 1; Fig. 2A-F). Overall, this indicated that independent of the mechanism of bleb formation, higher-order chromatin organization within blebs was associated with a lower-likelihood of well-formed packed domains (low *D*) and fragmented clutches (decreased FMM) with increased mobility (D_e) compared to the nuclear body. Comparing the observed behavior of chromatin domains across the nuclei in these conditions, we observed that inhibition of with GSK343 or TSA resulted in decreased D and FMM (Fig. 2F,G) in comparison to untreated controls.

Strikingly, even though higher-order chromatin structure within blebs was similar in all states compared to the nuclear body, the transformation of chromatin within the body was distinct for each mechanism. Specifically, B-type lamin depletion was associated with an increase in D and FMM compared to control cells (Fig. 2B,C) whereas inhibition of heterochromatin enzymes resulted in low *D* compared to their respective controls (Fig. 2F,G). This indicated that disruption of heterochromatin enzymatic processes produced chromatin domain fragmentation that was not occurring with B-type lamin depletion. Next, we compared the behavior of chromatin domains within blebs across all conditions. We unexpectedly observed that domains associated due to B-type lamin depletion had a comparably higher *D* and FMM compared to those that occur due to inhibition of heterochromatin remodeling enzymes (Fig. 2B,C,F,G; Fig. S1A,B). When paired with the findings in the nuclear body of each respective perturbation, this suggests a potential differential mechanism of bleb translocation for each model. Specifically, heterochromatin inhibition may be producing smaller domains that are spontaneously passing through smaller initial deformation of the nucleus. By contrast, the disruption of the lamina may be resulting in larger membrane defects that facilitate the passage of otherwise stable domains.

To further characterize the temporal dynamics of nuclear blebbing induced by either B-type lamin loss or heterochromatin disruption, we used dual-PWS to measure the mobility of mass between nuclear bleb and nuclear body in live cells. As TSA treatment resulted in the most substantial increase in the frequency of nuclear blebs

above, we treated HCT116$^{LMN(B1\&B2)\text{-}AID}$ cells with either DMSO or TSA. By measuring the spectral interference at a single wavelength as a function of time from within nuclei and within blebs, we could directly image and measure how mass was transitioning between these spaces (Gladstein et al., 2019). An advantage of this approach is that it can account for the transfer of both chromatin and non-chromatin proteins which would otherwise be challenging to quantify concurrently. As discussed above, variations in the temporal interference quantifies the FMM while the temporal-average signal is inversely proportional to the chromatin volume concentration (chromatin density) and the density of other nuclear macromolecules (Eid et al., 2020; Gladstein et al., 2019). Chromatin volume concentration (CVC), as the name implies, describes how chromatin occupies the volume on a relative scale of 0 to 1. Two examples of relative CVC that are seen in our analysis are illustrated in Fig. 3F.

Utilizing this approach, we can visualize the temporal evolution of density in both the nucleus and the bleb with a very high temporal resolution of 50 ms per frame (acquired over 15 s total in this instance). On imaging chromatin motion in the DMSO control nuclei, it is visually apparent that density moves randomly within the nucleus at short timescales (Movies 1-3). In contrast, within a TSA treated cell with a visually apparent bleb, density decreases rapidly adjacent to the nuclear bleb (Fig. 3A,B; Movies 1-3). In the TSA treated case (Fig. 3A **bottom**), we observe transit of small amounts of mass between the nuclear bleb and the main nuclear body. This is evidenced by an increased local density and the temporally evolving density in the bleb **(**Fig. 3A **TSA t:1/200->t:200/200)**. When measuring the relative CVC change over time in individual cells, we see that there is a heterogeneity when looking at both nuclear body and bleb regions of interest (Fig. 3B**)**. Interestingly, in the population ensemble (average trendline fits±standard error), we observe a higher relatively higher CVC for nuclear body in the TSA treated case compared to the accompanying blebs (Fig. 3C **bottom)**.

In contrast, blebs occurring in control cells which showed the opposite trend, with higher local density relative to the adjacent nucleus. In the context that DNA density is decreased in blebs relative to the body (Bunner et al., 2024 preprint) and the disruption of domains as quantified by the observed *D* within blebs, this indicates that blebs may become enriched in other non-chromatin macromolecules. When looking at regional chromatin concentration for bleb and nuclear regions for DMSO Control and TSA, we observe an increase in density for both bleb and nuclear body in the TSA treated cells compared to the control (Fig. 3D). Given that *D* decreases throughout the nucleus in TSA treated cells, this finding suggests that unexpectedly, even as chromatin domains are destabilized, nuclear density may be increasing from the presence of other macromolecules. Directly looking at the CVC in bleb to nuclear body ratio for paired nuclei, we see that there is a lower bleb to body ratio for TSA treated case. Collectively, these findings demonstrate a destabilization of chromatin domains within blebs with a concurrent accumulation in non-chromatin macromolecules.

Super-resolution imaging of chromatin heterochromatin clusters in nuclear blebs

Nuclear lamins and heterochromatin have been shown to act in parallel to maintain the mechanical properties of the nucleus but the consequence of these on chromatin nanodomains in bleb formation have not been investigated (Hoskins et al., 2021; Nava et al., 2020; Stephens et al., 2019b). Additionally, chromatin structure and dynamics are

often closely related, which may support mechanisms of either granting or limiting access to regions with high local chromatin concentration (Barth et al., 2020). In the context of prior work suggesting that chromatin domains are composed of high-density, presumably heterochromatic centers (Li et al., 2022, 2021; Miron et al., 2020; Szabo et al., 2020), we investigated the transformation in constitutive heterochromatin domains between the nuclear bleb and the nuclear body in spontaneously forming blebs (controls), in lamin B1/B2 depletion-associated blebs, and in heterochromatin enzyme-inhibited blebs (TSA) using Single Molecule Localization Microscopy. Single Molecule Localization Microscopy (SMLM) is a super-resolution imaging technique that allows for the precise localization of individual fluorescent molecules, achieving spatial resolutions beyond the diffraction limit of light. This method enables detailed visualization of molecular structures and interactions within cells, providing insights into biological processes at the nanoscale. A specific version of this technique STORM (stochastic optical reconstruction microscopy) was used to image chromatin, specifically allowing us to differentiate between distinct structures within a diffraction limited volume or the ensemble behavior of mass. In the manuscript, we chose to image the positioning of H3K9me3 as its associated with high-density regions that are observed to form the centroids of domain cores on electron microscopy. By pairing this with dual-PWS microscopy, we can investigate both the ensemble behavior of chromatin throughout the nucleus and the nanoscopic structure of high-density regions formed by heterochromatin. This is achieved with its high resolution capable of resolving nanoscopic structures between 10-30 nm. Due to the limitation of bleb formation being a low-frequency process (<15% of the time) (Table S1), we were only able to identify blebs in a few nuclei in total in HCT-116 cells (Fig. 4B-D). Given this limitation, we utilized a second cell-line model, U2OS cells, that were associated with higher rates of bleb formation upon HDAC inhibition with TSA (Fig. 5).

Visually, we observed distinct differences in H3K9me3 chromatin nanodomains (Fig. 4A) in these three conditions. In blebs formed spontaneously (Fig. 4B), blebs formed in B-type lamin depletion (Fig. 4C), and blebs formed due to inhibition of histone deacetylases (Fig. 4D), it is visually apparent that nanoscopic heterochromatin domains are observed. Within the nuclear body, as previously demonstrated (Pujadas et al., 2023 preprint; Pujadas Liwag et al., 2024), auxin-induced depletion of B-type lamins resulted in reduced peripheral heterochromatic cores at the nuclear periphery, however, domains formed within the nuclear interior were typically larger in size (Fig. 4E-G). With respect to heterochromatin nanodomains in GSK343 treated HCT116 cells (Pujadas et al., 2023 preprint; Pujadas Liwag et al., 2024) and TSA treated U2OS cells, these were smaller than those in control cells and in lamin B-depletion as expected due to the inhibition of heterochromatin enzymes within the nuclear body (Fig. 4E-G; Fig. 5C). In contrast to prior work, we found that the nuclear blebs arising from either B-type lamin degradation or TSA treatment contained heterochromatin around the periphery of blebs and within the center of the bleb (Fig. 4B,C,D; Fig. 5A,B). This finding highly contradicts the plethora of research stating that all nuclear blebs are devoid of heterochromatin (Bercht Pfleghaar et al., 2015; Helfand et al., 2012; Lammerding et al., 2006). Instead, these results show that independent B-type lamin loss, TSA treatment gives rise to non-canonical nuclear blebs enriched in heterochromatin around near their boundaries and the transfer of nanoscopic heterochromatin domains into the bleb. This also challenges the notion that euchromatin enrichment is the most reliable marker of nuclear

blebs (Bunner et al., 2024 preprint), and further suggests that other cellular mechanisms could play a role in the morphological properties of these herniations.

DISCUSSION

In this work, we found that nuclear packing domains are transformed within blebs induced by the loss of either B-type lamins or inhibition of heterochromatin enzymes. Specifically, the domains observed within blebs were typically poorly formed, with increased fragmentation and a higher effective diffusion coefficient compared to the domains observed in the nuclear body independent of the conditions. Despite the similarities across groups, we saw that domains associated with lamin B depletion were likely larger than those produced by inhibition of heterochromatin remodeling enzymes (GSK343 inhibition of EZH2 and TSA inhibition of HDACs) suggesting that the barrier to movement of domains or nucleosome clutches is larger in the loss of b-type lamins whereas the inhibition of heterochromatin enzymes fragments domains to facilitate blebbing in the nuclear border (Fig. 2A,E). Given these findings, one possible and interesting explanation is that the size of domains influences their likelihood to transit through temporally evolving defects in the nuclear envelope. In the absence of b-type lamins, such defects are potentially more likely to have a larger cavity, facilitating the transit of domains that would be too large to transfer in control cells. As such, depletion of b-type lamins may increase the frequency of large barrier disruption events or potentially result in larger transient defects that allow passage of larger domains into the bleb body. Further supporting these findings were the observation that the structure of heterochromatin clusters upon B-type lamin depletion are larger in size compared to those in nuclei treated with heterochromatin enzyme inhibitors on super-resolution microscopy (Fig. 4F,G) within the nuclear body. Likewise, although limited by the low frequency of bleb events, domains observed within all blebs were smaller in size and more disperse than those observed in the adjacent nuclear body, indicating that domain size is a potential consideration in the likelihood of bleb formation (Figs 4, 5).

The changes observed in chromatin domains within blebs could be related to functional consequences in signaling, possibly arising from applied mechanical stress when the nuclear lamina or heterochromatin are disrupted. For example, using single-nucleus isolation and micromanipulation assays, we previously demonstrated that nuclei with reduced heterochromatin levels are softer and succumb to nuclear blebbing, while nuclei with more heterochromatin levels are stiffer and resist blebbing (Stephens et al., 2018). This chromatin histone-modification-based nuclear rigidity could be related to the differential transcriptional responsiveness (i.e. transcriptional plasticity) previously observed in low- versus high-chromatin packing areas upon exposure to external stressors (Virk et al., 2020). In many cases, nuclear blebbing is a marker of cell death (i.e. apoptosis) and is often observed during normal developmental processes or in response to various extracellular stressors. The transformation of domains within blebs upon either B-type lamin or heterochromatin enzyme disruption could potentially accelerate these processes by increasing DNA damage or cytoskeletal reorganization. Alternatively, the observation that density across the nucleus increases even as domain structure fragments indicates that pressure may accumulate from the mobilization

of non-chromatin bound macromolecules. Bleb formation could in this case be a necessary event to maintain the stability of the remaining chromatin domains to ensure their continued cellular function (Fig. 3).

Although loss of B-type lamins and inhibition of heterochromatin enzymes both induced nuclear morphological changes and increased FMM within nuclear blebs, it is important to consider that these perturbations may not always reflect the same changes in cell phenotype. While B-type lamins are required for proper spatial positioning of heterochromatin and gene-specific loci (Chang et al., 2022; Pujadas et al., 2023 preprint; Pujadas Liwag et al., 2024), B-type lamin loss and heterochromatin disruption may impact different cellular mechanisms that give rise to these morphological changes. For example, in previous work, we found that decreasing heterochromatin promoted decreased nuclear rigidity and increased nuclear blebbing without necessarily altering lamins (Stephens et al., 2018). Conversely, removal of B-type lamins resulted in both a reduction of heterochromatin and increased nuclear blebbing (Chang et al., 2022; Pujadas et al., 2023 preprint; Pujadas Liwag et al., 2024). Therefore, while lamins and heterochromatin interact, depletion of either could have differential effects on chromatin organization. In this work, we also found that TSA or GSK343 treatment promoted more nuclear blebs in comparison to auxin treatment to remove B-type lamins. Although combined treatment of either auxin and TSA or auxin and GSK343 did not result in a statistically significant increase in these bleb frequency in comparison to TSA or GSK343 alone, our results were similar previous findings that conclude disruption of chromatin alone is sufficient to cause nuclear blebbing (Stephens et al., 2018). However, the distortions in the nucleus caused in part by the breakdown of connections between chromatin and the nuclear lamina may be intensified by pressure gradients resulting from external influences (Cao et al., 2016).

These external factors, such as confinement imposed by the actin cytoskeleton or the surrounding environment, could further contribute to the increased deformation of the nucleus. Additionally, processes such as HDACi or HMTi could act by expanding the volume of heterochromatin centers or destabilizing packing domains altogether. In theory, as weak, unstable packing domain (i.e. nascent domain) cores expand in size, one possible consequence could be increased variations in temporally active processes, such as gene transcription, resulting in amplified chromatin motion. Consequently, modifications to higher-order chromatin assemblies could promote bleb formation by degrading packing domains and/ or altering chromatin-based nuclear mechanics. However, further assessment is needed to confirm this theoretical interplay between packing domain formation, nuclear mechanics, and transcription.

The complexity of interactions within the genome results in varying chromatin dynamics at different length scales. Intrinsic characteristics of chromatin, which involve the dynamic rearrangement of histones, interactions among chromosome segments, chromatin remodelers, replication proteins, and transcriptional regulators are required for proper spatiotemporal genome organization. Other than Dual-PWS, several techniques have been utilized to investigate the contributions of chromatin dynamics to this organization. For example, a combination of photoactivated localization microscopy (PALM) and tracking of single nucleosomes was recently applied to assess nucleosome-nucleosome interactions and cohesin-RAD21 in domain formation and dynamics (Nozaki et al., 2017). In line with our results, TSA treatment increased chromatin dynamics. Recently, proximity ligation-based chromatin assembly assays have been applied to investigate the kinetics of nuclear lamina binding to newly replicated DNA in

mouse embryonic fibroblasts (Lovejoy et al., 2023). Finally, computational models have been applied to probe the time evolution of the chromatin over the G1 phase of the interphase in *Drosophila* that successfully predict dynamic positioning of all LADs at the nuclear envelope (Tolokh et al., 2023). While Chromatin Scanning Transmission Electron Microscopy (ChromSTEM) does not have live-cell imaging capabilities to resolve chromatin mobility (Li et al., 2022), future work may involve this high-resolution imaging technique to investigate how the shift in chromatin dynamics seen here could be related to shifts in chromatin density, volume, and shape.

MATERIALS AND METHODS

HCT116 cell culture

HCT116$^{LMN(B1\&B2)\text{-}AID}$ cells and U2OS cells were grown in McCoy's 5A Modified Medium (#16600-082, Thermo Fisher Scientific, Waltham, MA) supplemented with 10% FBS (#16000-044, Thermo Fisher Scientific, Waltham, MA) and penicillin-streptomycin (100 µg/ml; #15140-122, Thermo Fisher Scientific, Waltham, MA). To create these cells, HCT116 cells (ATCC, #CCL-247) were tagged with the AID system as previously described (Pujadas et al., 2023 preprint). All cells were cultured under recommended conditions at 37°C and 5% CO_2. All cells in this study were maintained between passage 5 and 20. Cells were allowed at least 24 h to re-adhere and recover from trypsin-induced detachment. All imaging was performed when the surface confluence of the dish was between 40–70%. All cells were tested for mycoplasma contamination (ATCC, #30-1012K) before starting perturbation experiments, and they have given negative results.

Auxin treatment

HCT116$^{LMN(B1\&B2}$)-AID cells were plated at 50,000 cells per well of a 6-well plate (Cellvis, P12-1.5H-N). To induce expression of OsTIR1, 2 µg/ml of doxycycline (Fisher Scientific, #10592-13-9) was added to cells 24 h prior to auxin treatment. 1000 µM Indole-3-acetic acid sodium salt (IAA, Sigma Aldrich, #6505-45-9) was solubilized in RNase-free water (Fisher Scientific, #10-977-015) before each treatment as a fresh solution and added to HCT116$^{LMN(B1\&B2)\text{-}AID}$ cells.

GSK343 treatment

HCT116$^{LMN(B1\&B2)\text{-}AID}$ cells were plated at 50,000 cells per well of a 6-well plate (Cellvis, P12-1.5H-N). Cells were given at least 24 h to re-adhere before treatment. GSK343 (Millipore Sigma, #SML0766) was dissolved in DMSO to create a 10 mM stock solution. This was further diluted in complete cell media to a final treatment concentration of 10 µM. An equivalent final concentration of DMSO in media was used for the control group such that DMSO was diluted in media and added to cells in a 0.1% v/v ratio.

Trichostatin A (TSA) treatment

HCT116$^{LMN(B1\&B2)\text{-}AID}$ cells were plated at 50,000 cells per well of a 6-well plate (Cellvis, P12-1.5H-N). Cells were given at least 24 h to re-adhere before treatment. TSA (Millipore Sigma, #T1952) was diluted in complete cell medium and added to cells at a final treatment concentration of 300 nM. A final concentration of 0.1% v/v of DMSO was used as a control for this drug treatment.

Immunofluorescence sample preparation

HCT116$^{LMN(B1\&B2)\text{-}AID}$ cells at a low passage (<P10) were plated at 100,000 cells per well of a 6-well glass-bottom plate (Cellvis, #P06-1.5H-N). Following auxin treatment, cells were washed twice with 1× Phosphate Buffered Saline (PBS) (Gibco, #10010031). Cells were fixed with 4% paraformaldehyde (PFA) (Electron Microscopy Sciences, #15710) for 10 min at room temperature, followed by washing with PBS 3 times for 5 min each. Cells were permeabilized using 0.2% TritonX-100 (10%) (Sigma-Aldrich, #93443) in 1× PBS, followed by another wash with 1× PBS for 3 times for 5 min each. Cells were blocked using 3% BSA (Sigma-Aldrich, #A7906) in PBST (Tween-20 in 1× PBS) (Sigma-Aldrich, #P9416) at room temperature. The following primary antibodies were added overnight at 4°C: anti-H3K27ac (Abcam, #ab177178, dilution 1:7000) and anti-H3K27me3 (Abcam, #ab6002, dilution 1:200). Cells were washed with 1× PBS 3 times for 5 min each. The following secondary antibodies were added for 1 h at room temperature: Goat anti-Rabbit IgG (H+L) Alexa Fluor 568 (Abcam, #ab175471, dilution 1:1000) and Goat anti-Mouse IgG (H+L) Highly Cross-Adsorbed Secondary Antibody, Alexa Fluor Plus 647 (Thermo Fisher Scientific, #A32728, dilution 1:200). Cells were washed with 1× PBS 3 times for 5 min each. Finally, cells were stained with DAPI (Thermo Fisher Scientific, #62248, diluted to 0.5 µg/ml in 1× PBS) for 10 min at room temperature. Prior to imaging, cells were washed with 1× PBS twice for 5 min each.

Immunofluorescence imaging

Live and fixed cells were imaged using the Nikon SoRa Spinning Disk confocal microscope equipped with a Hamamatsu ORCA-Fusion Digital CMOS camera. Live cells were imaged under physiological conditions (37°C and 5% CO_2) using a stage top incubator (Tokai Hit). Images were collected using a 60×/1.42 NA oil-immersion objective mounted with a 2.8× magnifier. mClover was excited with a 488 nm laser, Alexa Fluor 647 was excited with a 640 nm laser, and DAPI was excited with a 405 nm laser. Imaging data were acquired by Nikon acquisition software.

Dual-PWS imaging

For live-cell measurements, cells were imaged and maintained under physiological conditions (5% CO^2 and 37°C) using a stage-top incubator (In Vivo Scientific, Salem, SC; Stage Top Systems). Live-cell PWS measurements were obtained using a commercial inverted microscope (Leica, DMIRB) using a Hamamatsu Image-EM charge-coupled

device (CCD) camera (C9100-13) coupled to a liquid crystal tunable filter (LCTF, CRi VariSpec) to acquire monochromatic, spectrally resolved images ranging from 500-700 nm at 2-nm intervals as previously described (Almassalha Luay et al., 2016; Gladstein et al., 2019, 2018). Broadband illumination was provided by a broad-spectrum white light LED source (Xcite-120 LED, Excelitas). The system is equipped with a long pass filter (Semrock BLP01-405R-25) and a 63× oil immersion objective (Leica HCX PL APO). All cells were given at least 24 h to re-adhere before treatment (for treated cells) and imaging. Briefly, PWS imaging is performed using a specialized microscope design that captures interference spectra resulting from the interaction between a reference wave and waves scattered from spatial refractive index variations within the coherence volume. The refractive index is proportional to the local chromatin density, which is linked to the 3D conformation of the chromatin polymer. The standard deviation of the interference spectra is proportional to the Fourier transform of the autocorrelation function of chromatin density integrated over the Fourier transform of the coherence volume. By analyzing the PWS image cubes (x,y,λ) calculating the standard deviation of pixel intensity across wavelengths, the local average chromatin packing scaling $D_a(x,y)$ can be determined for each (x,y) location within the nucleus. This calculation utilizes known optical parameters of illumination and signal acquisition, as well as the functional form of the chromatin density autocorrelation function previously measured by chromatin electron tomography. The nuclear average scaling D_n is then obtained by averaging Da(x,y) across the entire nucleus, providing a measure of the upregulation of chromatin domains within the nucleus (Eid et al., 2020; Gladstein et al., 2019; Li et al., 2021; Virk et al., 2020). Changes in D_n resulting from each condition are quantified by averaging cells, taken across 3 technical replicates. Average D_n was calculated by first averaging D_n values from PWS measurements within each cell nucleus and then averaging these measurements over the entire cell population for each treatment condition.

Dynamic PWS measurements

Temporal PWS data was acquired as previously described (Gladstein et al., 2019; Pujadas et al., 2023 preprint). Briefly, dynamics measurements (Σ_t^2 , fractional moving mass (m_f), and diffusion) are collected by acquiring multiple backscattered wide-field images at a single wavelength (550 nm) over time (acquisition time), to produce a three-dimensional image cube, where Σ_t^2 is temporal interference and t is time. Diffusion is extracted by calculating the decay rate of the autocorrelation of the temporal interference as previously described (Gladstein et al., 2019). The fractional moving mass is calculated by normalizing the variance of Σ_t^2 at each pixel. Using the equations and parameters supplied and explained in detail in the supplementary information of our recent publication (Gladstein et al., 2019), the fractional moving mass is obtained by using the following equation to normalize Σ_t^2 by ρ_0, the density of a typical macromolecular cluster:

$$\Sigma_t^2\left(\frac{\pi\rho_0}{2\Gamma^2k^3n_i}\right)\left(\frac{NA_i}{NA_c}\right)^2\left(\frac{n_1}{n_m-n_1}\right)^2=\rho_0 V_{cm}\varphi=m_c\varphi=m_f \qquad (1)$$

With this normalization, Σ_t^2 is equivalent to m_f, which measures the mass moving within the sample. This value is calculated from the product of the mass of the typical moving cluster (m_c) and the volume fraction of mobile mass (φ). m_c is obtained by $m_c = V_{cm}\rho_0$, where V_{cm} is the volume of the typical moving macromolecular cluster. To calculate this normalization, we approximate n_m =1.43 as the refractive index (RI) of a nucleosome, n_1 =1.37 as the RI of a nucleus, n_i =1.518 as the refractive index of the immersion oil, and ρ_0 =0.55 g cm^{-3} as the dry density of a nucleosome. Additionally, k =1.57E5 cm^{-1} is the scalar wavenumber of the illumination light and Γ is a Fresnel intensity coefficient for normal incidence. NA_c =1.49 is the numerical aperture (NA) of collection and NA_i =0.52 is the NA of illumination. As stated previously (Gladstein et al., 2019), Σ_t^2 is sensitive to instrument parameters such as the depth of field, substrate refractive index, etc. These dependencies are removed through normalization with the proper pre-factor calculated above for obtaining biological measurements. It should also be noted that backscattered intensity is prone to errors along the transverse direction (Gladstein et al., 2019). Due to these variations, these parameters are more accurate when calculating the expected value over each pixel.

Chromatin volume concentration is calculated by Fresnel reflection coefficient. Recall that the reflectance at a RI mismatch interface:

$$R_s = \left|\frac{n_1\cos\theta_i - n_2\cos\theta_t}{n_1\cos\theta_i + n_2\cos\theta_t}\right|^2 = \left|\frac{n_1\cos\theta_i - n_2\sqrt{1-\left(\frac{n_1}{n_2}\sin\theta_i\right)^2}}{n_1\cos\theta_i + n_2\sqrt{1-\left(\frac{n_1}{n_2}\sin\theta_i\right)^2}}\right|^2. \quad (2)$$

$$R_p = \left|\frac{n_1\cos\theta_t - n_2\cos\theta_i}{n_1\cos\theta_t + n_2\cos\theta_i}\right|^2 = \left|\frac{n_1\sqrt{1-\left(\frac{n_1}{n_2}\sin\theta_i\right)^2} - n_2\cos\theta_i}{n_1\sqrt{1-\left(\frac{n_1}{n_2}\sin\theta_i\right)^2} + n_2\cos\theta_i}\right|^2. \quad (3)$$

Although the chromatin is inhomogeneous and not infinitely large, the correlation between chromatin average RI and reflection coefficients still holds as confirmed by Finite Difference Time Domain (FDTD) simulations (Fig. S3). Briefly, we used home-built FDTD software to simulate the entire PWS imaging system, from incident to light-matter interaction and then collection (Çapoğlu et al., 2013). Light beams representing the characteristics of experimental NA_i are first introduced to the simulation space. The simulation space contains a layer of glass and random media that represents chromatin average RI and packing behavior. The EM wave after light-matter interaction is then collected with the same NA_c and far field PWS image is analyzed the same way in experiments.

We did a series of simulations with different average RI and measured the mean reflection coefficients. We have fitted:

$$\frac{R}{R_0} = 0.36\phi^2 - 1.1\phi + 1.0 \tag{4}$$

where ϕ is chromatin volume concentration, related to RI through Gladstone-Dale equation (Gladstein et al., 2019; Virk et al., 2020):

$$n_{nucleus} = 1.3446 + 0.0882\phi. \tag{5}$$

Normalization of Dynamics PWS Data

Normalization for data seen in Fig. 3 is done in two ways. For single cell region of interest Relative CVC change over time, the data is normalized to a range of 0,1. This is done by calculating: $\frac{I(x,y,t)}{I_0(x,y,t)}$ for the entire field of view, where I_0 is from the reference image taken during all PWS dynamics experiments. We then take the inverse and normalize the data range to fall within 0-1. The ensemble is the average of the results applied to all cell regions of interest for a given treatment condition. The second normalization method is acquired by first calculating the average intensity across all wavelengths for a given region of interest. Then using the established relationship between intensity and CVC we calculate the equivalent CVC value and convert it to range of 0 to 1.

SMLM sample preparation and imaging

Primary antibody rabbit anti-H3K9me3 (Abcam, #ab176916, dilution 1:1000) was aliquoted and stored at −80°C. The secondary antibody goat anti-rabbit AF647 (Thermo Fisher Scientific, #A-21245, dilution 1:1000) was stored at 4°C. The cells were plated on No. 1 borosilicate bottom eight-well Lab-Tek Chambered cover glass with at a seeding density of 1.25×10^4. After 48 h, the cells were fixed in 3% paraformaldehyde in PBS for 10 min, and then subsequently washed with PBS once for five minutes. Thereafter the samples were quenched with freshly prepared 0.1% sodium borohydride in PBS for 7 min and rinsed with PBS three times at room temperature. The fixed samples were permeabilized with a blocking buffer (3% bovine serum albumin (BSA), 0.5% Triton X-100 in PBS) for 20 min and then incubated with rabbit anti-H3K9me3 in blocking buffer for 1-2 h at room temperature and rinsed with a washing buffer (0.2% BSA, 0.1% Triton X-100 in PBS) three times. The fixed samples were further incubated with the corresponding goat secondary antibody–dye conjugates, anti-rabbit AF647, for 40 min, washed thoroughly with PBS three times at room temperature and stored at 4°C. Imaging of samples was performed on a STORM optical setup built on the commercially available Nikon Ti2 equipped with a Photometric 95B sCMOS camera and a 1.49 NA 100X oil immersion objective lens. Samples were illuminated with the MPB

Communications 2RU-VFL-P-2000-647-B1R 647 nm 200 mW laser. Image acquisition was performed at 20-30 ms exposure for 10-15 k frames.

Data and image analysis

We used GraphPad Prism 10.1.1 for making all plots. For immunofluorescence imaging, maximum intensity projection of Z-series images was performed using FIJI (Schindelin et al., 2012). To quantify nuclear bleb frequency, we considered blebs to be herniations that were still connected to the nuclear body. We considered ruptures to be cells that were no longer intact, and we considered micronuclei to be herniations that were no longer connected to the nuclear body and of similar sizes to nuclear blebs. For each field of view, the number of nuclei and the number of each nuclear bleb type was manually counted using FIJI. We then determined the percentages of total cells within each tested condition that displayed each nuclear bleb type.

Super-resolution data analysis

We used the Thunder-STORM FIJI Plug-in (Ovesný et al., 2014) to apply Maximum Likelihood Estimation fitting of a gaussian point spread function to our image stack. Localization datasets were then put into our Python script that utilized DBSCAN (epsilon=50, min_pts=3) to cluster our localized heterochromatic events. Heterochromatin domain size was estimated by fitting a polygon to the peripheral cluster points using the *scipy* Convex Hull method. Outlier clusters smaller than twice the mean uncertainty of our localization (~25 nm) or larger than 800 nm were removed from the analysis. Results displayed are concatenations of identified heterochromatic domains across all cells in that condition.

Statistical analysis and quantification

Statistical analysis was performed using GraphPad Prism 10.1.1 and Microsoft Excel. Pairwise comparisons were calculated on datasets consisting of, at a minimum, biologically independent duplicate samples using a two-tailed unpaired *t*-test or Mann–Whitney test. The type of statistical test is specified in each case. Experimental data are presented either the mean±s.e.m. or mean±s.d., as stated in figure legends. A P value of<0.05 was considered significant. Statistical significance levels are denoted as follows: n.s.=not significant; *P<0.05; **P<0.01; ***P<0.001; ****P<0.0001. Sample numbers (# of nuclei, n), the number of replicates (N), and the type of statistical test used is indicated in figure legends.

Acknowledgements

Microscopy was performed at the Biological Imaging Facility at Northwestern University (RRID:SCR_017767), graciously supported by the Chemistry for Life Processes Institute, the NU Office for Research, the Department of

Molecular Biosciences and the Rice Foundation. FDTD simulations were performed at Quest, a high-performance computing cluster at Northwestern University.

Competing interests

The authors declare no competing or financial interests.

Author contributions

E.M.P. and L.A. wrote the paper and performed immunofluorescence and Dual-PWS imaging and analysis. N.A. and L.A. conducted SMLM imaging and analysis. N.A. assisted with representative Dual-PWS images. Y.S. conducted density estimations from Dual-PWS data. R.G. set up the optical system for all super-resolution image acquisition. E.M.P, A.S., L.A., and V.B. conceptualized the project and edited the manuscript.

Funding

This work was supported by NSF grants EFMA-1830961 and EFMA-1830969 and NIH grants R01CA228272, U54 CA268084, and U54 CA261694. L.A. was supported by the NIH Training Grant T32AI083216. ADS was funded by the National Institutes of Health Pathway to Independence Award (R00GM123195) and the National Institutes of Health Center for 3D Structure and Physics of the Genome 4DN2 grant (1UM1HG011536). Philanthropic support was generously received from Rob and Kristin Goldman, the Christina Carinato Charitable Foundation, Mark E. Holliday and Mrs. Ingeborg Schneider, and Mr. David Sachs. Open Access funding provided by Northwestern University. Deposited in PMC for immediate release.

Data availability

All relevant data can be found at the Dyad repository (https://doi.org/10.5061/dryad.gb5mkkx0d) The cell lines have been authenticated and are available upon request. Further information and requests for resources and reagents should be directed to and will be fulfilled by the lead contact, Vadim Backman (v-backman@northwestern.edu).

Diversity and inclusion statement

One or more of the authors of this paper self-identifies as an underrepresented minority.

References

Almassalha Luay, M., Bauer Greta, M., Chandler John, E., Gladstein, S., Cherkezyan, L., Stypula-Cyrus, Y., Weinberg, S., Zhang, D., Thusgaard Ruhoff, P. and Roy Hemant, K. (2016). Label-free imaging of the native, living cellular nanoarchitecture using partial-wave spectroscopic microscopy. *Proc. Natl. Acad. Sci. USA* 113, E6372-E6381. doi:10.1073/pnas.1521269113

Barth, R., Bystricky, K. and Shaban, H. A. (2020). Coupling chromatin structure and dynamics by live super-resolution imaging. *Sci. Adv.* 6, eaaz2196. doi:10.1126/sciadv.aaz2196

Bercht Pfleghaar, K., Taimen, P., Butin-Israeli, V., Shimi, T., Langer-Freitag, S., Markaki, Y., Goldman, A. E., Wehnert, M. and Goldman, R. D. (2015). Gene-rich chromosomal regions are preferentially localized in the lamin B deficient nuclear blebs of atypical progeria cells. *Nucleus* 6, 66-76. doi:10.1080/19491034.2015.1004256

Berg, I. K., Currey, M. L., Gupta, S., Berrada, Y., Nguyen, B. V., Pho, M., Patteson, A. E., Schwarz, J. M., Banigan, E. J. and Stephens, A. D. (2023). Transcription inhibition suppresses nuclear blebbing and rupture independently of nuclear rigidity. *J. Cell Sci.* 136, jcs261547. doi:10.1242/jcs.261547

Bunner, S., Prince, K., Srikrishna, K., Pujadas, E. M., Pellegrino, P., Aiello, J., McCarthy, A. A., Lawlor, C., Jagtap, S., Kuklinski, A. et al. (2024). DNA density is a better indicator of a nuclear bleb than lamin B loss. *bioRxiv*. doi:10.1242/jcs.262082

Burke, B. and Stewart, C. L. (2013). The nuclear lamins: flexibility in function. *Nat. Rev. Mol. Cell Biol.* 14, 13-24. doi:10.1038/nrm3488

Cao, X., Moeendarbary, E., Isermann, P., Davidson, P. M., Wang, X., Chen, M. B., Burkart, A. K., Lammerding, J., Kamm, R. D. and Shenoy, V. B. (2016). A chemomechanical model for nuclear morphology and stresses during cell transendothelial migration. *Biophys. J.* 111, 1541-1552. doi:10.1016/j.bpj.2016.08.011

Çapoğlu, I. R., Allen, T. and Backman, V. (2013). Angora: a free software package for finite-difference time-domain electromagnetic simulation. *IEEE Antennas Propag. Mag.* 55, 80-93. doi:10.1109/MAP.2013.6645144

Chang, L., Li, M., Shao, S., Li, C., Ai, S., Xue, B., Hou, Y., Zhang, Y., Li, R., Fan, X. et al. (2022). Nuclear peripheral chromatin-lamin B1 interaction is required for global integrity of chromatin architecture and dynamics in human cells. *Protein Cell* 13, 258-280. doi:10.1007/s13238-020-00794-8

Chen, N. Y., Kim, P., Weston, T. A., Edillo, L., Tu, Y., Fong, L. G. and Young, S. G. (2018). Fibroblasts lacking nuclear lamins do not have nuclear blebs or protrusions but nevertheless have frequent nuclear membrane ruptures. *Proc. Natl. Acad. Sci. USA* 115, 10100-10105. doi:10.1073/pnas.1812622115

Chiu, K., Berrada, Y., Eskndir, N., Song, D., Fong, C., Naughton, S., Chen, T., Moy, S., Gyurmey, S., James, L. et al. (2024). CTCF is essential for proper mitotic spindle structure and anaphase segregation. *Chromosome* 133, 183-194. doi:10.1007/s00412-023-00810-w

Currey, M. L., Kandula, V., Biggs, R., Marko, J. F. and Stephens, A. D. (2022). A versatile micromanipulation apparatus for biophysical assays of the cell nucleus. *Cell Mol. Bioeng.* 15, 303-312.

Dupouy, G., Dong, Y., Herzog, E., Chabouté, M.-E. and Berr, A. (2024). Nuclear envelope dynamics in connection to chromatin remodeling. *Plant J.* 118, 963-981. doi:10.1111/tpj.16246

Eid, A., Eshein, A., Li, Y., Virk, R., Van Derway, D., Zhang, D., Taflove, A. and Backman, V. (2020). Characterizing chromatin packing scaling in whole nuclei using interferometric microscopy. *Opt. Lett.* 45, 4810-4813. doi:10.1364/OL.400231

Evangelisti, C., Rusciano, I., Mongiorgi, S., Ramazzotti, G., Lattanzi, G., Manzoli, L., Cocco, L. and Ratti, S. (2022). The wide and growing range of lamin B-related diseases: from laminopathies to cancer. *Cell. Mol. Life Sci.* 79, 126. doi:10.1007/s00018-021-04084-2

Funkhouser, C. M., Sknepnek, R., Shimi, T., Goldman, A. E., Goldman, R. D. and Olvera De La Cruz, M. (2013). Mechanical model of blebbing in nuclear lamin meshworks. *Proc. Natl. Acad. Sci. USA* 110, 3248-3253. doi:10.1073/pnas.1300215110

Gladstein, S., Stawarz, A., Almassalha, L. M., Cherkezyan, L., Chandler, J. E., Zhou, X., Subramanian, H. and Backman, V. (2018). Measuring nanoscale chromatin heterogeneity with partial wave spectroscopic microscopy. *Methods Mol. Biol.* 1745, 337-360. doi:10.1007/978-1-4939-7680-5_19

Gladstein, S., Almassalha, L. M., Cherkezyan, L., Chandler, J. E., Eshein, A., Eid, A., Zhang, D., Wu, W., Bauer, G. M., Stephens, A. D. et al. (2019). Multimodal interference-based imaging of nanoscale structure and macromolecular motion uncovers UV induced cellular paroxysm. *Nat. Commun.* 10, 1652. doi:10.1038/s41467-019-09717-6

Hatch, E. M. and Hetzer, M. W. (2016). Nuclear envelope rupture is induced by actin-based nucleus confinement. *J. Cell Biol.* 215, 27-36. doi:10.1083/jcb.201603053

Helfand, B. T., Wang, Y., Pfleghaar, K., Shimi, T., Taimen, P. and Shumaker, D. K. (2012). Chromosomal regions associated with prostate cancer risk localize to lamin B-deficient microdomains and exhibit reduced gene transcription. *J. Pathol.* 226, 735-745. doi:10.1002/path.3033

Hoskins, V. E., Smith, K. and Reddy, K. L. (2021). The shifting shape of genomes: dynamics of heterochromatin interactions at the nuclear lamina. *Curr. Opin. Genet. Dev.* 67, 163-173. doi:10.1016/j.gde.2021.02.003

Jung-Garcia, Y., Maiques, O., Monger, J., Rodriguez-Hernandez, I., Fanshawe, B., Domart, M. C., Renshaw, M. J., Marti, R. M., Matias-Guiu, X., Collinson, L. M. et al. (2023). LAP1 supports nuclear adaptability during constrained melanoma cell migration and invasion. *Nat. Cell Biol.* 25, 108-119. doi:10.1038/s41556-022-01042-3

Kalukula, Y., Stephens, A. D., Lammerding, J. and Gabriele, S. (2022). Mechanics and functional consequences of nuclear deformations. *Nat. Rev. Mol. Cell Biol.* 23, 583-602. doi:10.1038/s41580-022-00480-z

Karoutas, A. and Akhtar, A. (2021). Functional mechanisms and abnormalities of the nuclear lamina. *Nat. Cell Biol.* 23, 116-126. doi:10.1038/s41556-020-00630-5

Lammerding, J., Fong, L. G., Ji, J. Y., Reue, K., Stewart, C. L., Young, S. G. and Lee, R. T. (2006). Lamins A and C but not Lamin B1 regulate nuclear mechanics. *J. Biol. Chem.* 281, 25768-25780. doi:10.1074/jbc.M513511200

Le Berre, M., Aubertin, J. and Piel, M. (2012). Fine control of nuclear confinement identifies a threshold deformation leading to lamina rupture and induction of specific genes. *Integr. Biol. (Camb)* 4, 1406-1414. doi:10.1039/c2ib20056b

Li, Y., Eshein, A., Virk, R. K. A., Eid, A., Wu, W., Frederick, J., Vanderway, D., Gladstein, S., Huang, K., Anthony, N. M. et al. (2021). Nanoscale chromatin imaging and analysis (nano-ChIA) platform bridges 4-D chromatin organization with molecular function. *Sci. Adv.* 7, eabe4310. doi:10.1126/sciadv.abe4310

Li, Y., Agrawal, V., Virk, R. K. A., Roth, E., Li, W. S., Eshein, A., Frederick, J., Huang, K., Almassalha, L., Bleher, R. et al. (2022). Analysis of three-dimensional chromatin packing domains by chromatin scanning transmission electron microscopy (ChromSTEM). *Sci. Rep.* 12, 12198. doi:10.1038/s41598-022-16028-2

Lochs, S. J. A., Kefalopoulou, S. and Kind, J. (2019). Lamina associated domains and gene regulation in development and cancer. *Cells* 8, 271. doi:10.3390/cells8030271

Lovejoy, C. M., Nagarajan, P. and Parthun, M. R. (2023). Dynamic reassociation of the nuclear lamina with newly replicated DNA. *Res. Square*. doi:10.21203/rs.3.rs-2846826/v1

Miron, E., Oldenkamp, R., Brown, J. M., Pinto, D. M. S., Xu, C. S., Faria, A. R., Shaban, H. A., Rhodes, J. D. P., Innocent, C., De Ornellas, S. et al. (2020). Chromatin arranges in chains of mesoscale domains with nanoscale functional topography independent of cohesin. *Sci. Adv.* 6, eaba8811. doi:10.1126/sciadv.aba8811

Mistriotis, P., Wisniewski, E. O., Bera, K., Keys, J., Li, Y., Tuntithavornwat, S., Law, R. A., Perez-Gonzalez, N. A., Erdogmus, E., Zhang, Y. et al. (2019). Confinement hinders motility by inducing RhoA-mediated nuclear influx, volume expansion, and blebbing. *J. Cell Biol.* 218, 4093-4111. doi:10.1083/jcb.201902057

Nava, M. M., Miroshnikova, Y. A., Biggs, L. C., Whitefield, D. B., Metge, F., Boucas, J., Vihinen, H., Jokitalo, E., Li, X., García Arcos, J. M. et al. (2020). Heterochromatin-driven nuclear softening protects the genome against mechanical stress-induced damage. *Cell* 181, 800-817.e22. doi:10.1016/j.cell.2020.03.052

Nmezi, B., Xu, J., Fu, R., Armiger Travis, J., Rodriguez-Bey, G., Powell Juliana, S., Ma, H., Sullivan, M., Tu, Y., Chen Natalie, Y. et al. (2019). Concentric organization of A- and B-type lamins predicts their distinct roles in the spatial organization and stability of the nuclear lamina. *Proc. Natl. Acad. Sci. USA* 116, 4307-4315. doi:10.1073/pnas.1810070116

Nozaki, T., Imai, R., Tanbo, M., Nagashima, R., Tamura, S., Tani, T., Joti, Y., Tomita, M., Hibino, K., Kanemaki, M. T. et al. (2017). Dynamic organization of chromatin domains revealed by super-resolution live-cell imaging. *Mol. Cell* 67, 282-293.e7. doi:10.1016/j.molcel.2017.06.018

Ovesný, M., Křížek, P., Borkovec, J., Svindrych, Z. and Hagen, G. M. (2014). ThunderSTORM: a comprehensive ImageJ plug-in for PALM and STORM data analysis and super-resolution imaging. *Bioinformatics* 30, 2389-2390. doi:10.1093/bioinformatics/btu202

Pho, M., Berrada, Y., Gunda, A., Lavallee, A., Chiu, K., Padam, A., Currey, M. L. and Stephens, A. D. (2024). Actin contraction controls nuclear blebbing and rupture independent of actin confinement. *Mol. Biol. Cell* 35, ar19. doi:10.1091/mbc.E23-07-0292

Pujadas, E. M., Wei, X., Acosta, N., Carter, L., Yang, J., Almassalha, L., Daneshkhah, A., Rao, S. S. P., Agrawal, V., Seker-Polat, F. et al. (2023). Depletion of lamins B1 and B2 alters chromatin mobility and induces differential gene expression by a mesoscale-motion dependent mechanism. *bioRxiv*. doi:10.1101/2023.06.26.546573

Pujadas Liwag, E. M., Wei, X., Acosta, N., Carter, L. M., Yang, J., Almassalha, L. M., Jain, S., Daneshkhah, A., Rao, S. S. P., Seker-Polat, F. et al. (2024). Depletion of lamins B1 and B2 promotes chromatin mobility and induces differential gene expression by a mesoscale-motion-dependent mechanism. *Genome Biol.* 25, 77. doi:10.1186/s13059-024-03212-y

Qin, L., He, T., Chen, S., Yang, D., Yi, W., Cao, H. and Xiao, G. (2021). Roles of mechanosensitive channel Piezo1/2 proteins in skeleton and other tissues. *Bone Res.* 9, 44. doi:10.1038/s41413-021-00168-8

Schindelin, J., Arganda-Carreras, I., Frise, E., Kaynig, V., Longair, M., Pietzsch, T., Preibisch, S., Rueden, C., Saalfeld, S., Schmid, B. et al. (2012). Fiji: an open-source platform for biological-image analysis. *Nat. Methods* 9, 676-682. doi:10.1038/nmeth.2019

Stephens, A. D., Banigan, E. J., Adam, S. A., Goldman, R. D. and Marko, J. F. (2017). Chromatin and lamin A determine two different mechanical response regimes of the cell nucleus. *Mol. Biol. Cell* 28, 1984-1996. doi:10.1091/mbc.e16-09-0653

Stephens, A. D., Liu, P. Z., Banigan, E. J., Almassalha, L. M., Backman, V., Adam, S. A., Goldman, R. D. and Marko, J. F. (2018). Chromatin histone modifications and rigidity affect nuclear morphology independent of lamins. *Mol. Biol. Cell* 29, 220-233. doi:10.1091/mbc.E17-06-0410

Stephens, A. D., Banigan, E. J. and Marko, J. F. (2019a). Chromatin's physical properties shape the nucleus and its functions. *Curr. Opin. Cell Biol.* 58, 76-84. doi:10.1016/j.ceb.2019.02.006

Stephens, A. D., Liu, P. Z., Kandula, V., Chen, H., Almassalha, L. M., Herman, C., Backman, V., O'halloran, T., Adam, S. A., Goldman, R. D. et al. (2019b). Physicochemical mechanotransduction alters nuclear shape and mechanics via heterochromatin formation. *Mol. Biol. Cell* 30, 2320-2330. doi:10.1091/mbc.E19-05-0286

Szabo, Q., Donjon, A., Jerković, I., Papadopoulos, G. L., Cheutin, T., Bonev, B., Nora, E. P., Bruneau, B. G., Bantignies, F. and Cavalli, G. (2020). Regulation of single-cell genome organization into TADs and chromatin nanodomains. *Nat. Genet.* 52, 1151-1157. doi:10.1038/s41588-020-00716-8

Tolokh, I. S., Kinney, N. A., Sharakhov, I. V. and Onufriev, A. V. (2023). Strong interactions between highly dynamic lamina-associated domains and the nuclear envelope stabilize the 3D architecture of Drosophila interphase chromatin. *Epigene. Chromatin* 16, 21. doi:10.1186/s13072-023-00492-9

Vahabikashi, A., Sivagurunathan, S., Nicdao, F. A. S., Han, Y. L., Park, C. Y., Kittisopikul, M., Wong, X., Tran, J. R., Gundersen, G. G., Reddy, K. L. et al. (2022). Nuclear lamin isoforms differentially contribute to LINC complex-dependent nucleocytoskeletal coupling and whole-cell mechanics. *Proc. Natl. Acad. Sci. USA* 119, e2121816119. doi:10.1073/pnas.2121816119

Vargas, J. D., Hatch, E. M., Anderson, D. J. and Hetzer, M. W. (2012). Transient nuclear envelope rupturing during interphase in human cancer cells. *Nucleus* 3, 88-100. doi:10.4161/nucl.18954

Virk, R. K. A., Wu, W., Almassalha, L. M., Bauer, G. M., Li, Y., Vanderway, D., Frederick, J., Zhang, D., Eshein, A., Roy, H. K. et al. (2020). Disordered chromatin packing regulates phenotypic plasticity. *Sci. Adv.* 6, eaax6232. doi:10.1126/sciadv.aax6232

Yesbolatova, A., Natsume, T., Hayashi, K. I. and Kanemaki, M. T. (2019). Generation of conditional auxin-inducible degron (AID) cells and tight control of degron-fused proteins using the degradation inhibitor auxinole. *Methods* 164-165, 73-80. doi:10.1016/j.ymeth.2019.04.010

Figures and Tables

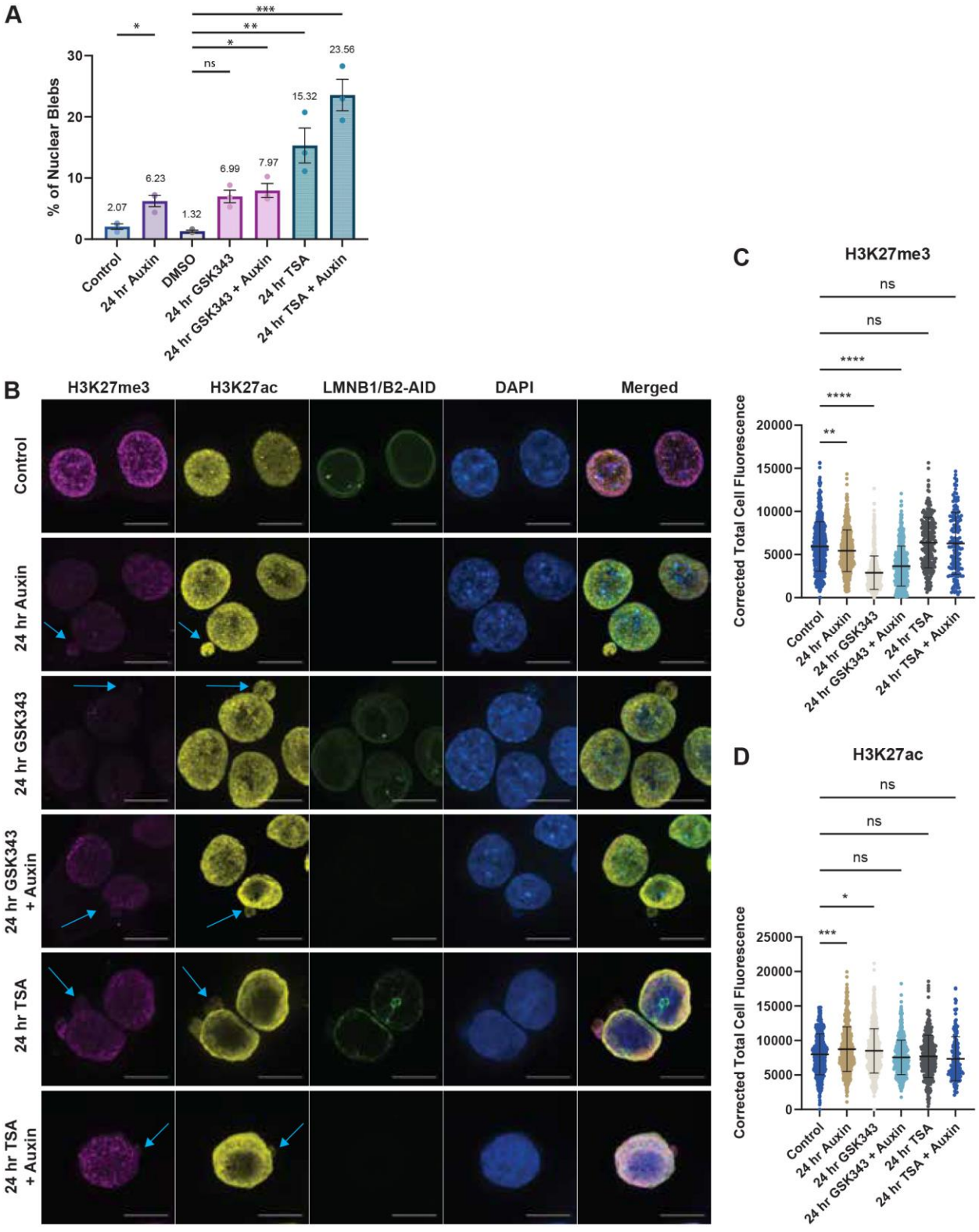

Fig. 1. Aberrant nuclear morphology is induced by the loss of B-type lamins or heterochromatin. (A) Percentages of nuclear blebs compiled over each field of view for untreated (control), 24-h auxin conditions in HCT116$^{LMN(B1\&B2)\text{-}AID}$ cells, DMSO, 24-hr GSK343, 24-hr TSA, 24-h GSK343 with auxin and 24-hr TSA with auxin. Each dot represents a technical replicate (N=3; Control n=1102, Auxin n=1081, DMSO n=295, GSK343 n=1096, TSA n=456, GSK343 + Auxin n=933, TSA + Auxin n=456). For (A), bar plots are represented as mean±SEM. Unpaired two-tailed t-test with Holm-Šídák test for multiple comparisons applied. (B) Representative confocal images of H3K27me3 (magenta), H3K27ac (yellow), Lamin B1/B2-AID (green), DAPI (blue), and merged fluorescence for control, 24-h auxin, 24-h GSK343, 24-h GSK343 + Auxin, 24-h TSA, and 24-h TSA + Auxin treatment conditions in HCT116$^{LMN(B1\&B2)\text{-}AID}$ cells. Scale bar=10 µm. Blue arrows indicate nuclear bleb deformations. (C) Corrected total cell fluorescence measurements of H3K27me3 and (D) H3K27ac for control, 24-h auxin, 24-h GSK343, 24-h GSK343 + Auxin, 24-h TSA, and 24-h TSA + Auxin treatment conditions in HCT116$^{LMN(B1\&B2)\text{-}AID}$ cells. Each dot represents a cell nucleus. Violin plots show the median and quartiles. Error bars represent mean±s.d. One-way ANOVA with Dunnett's test for multiple comparisons. For (C,D), data are representative of two technical replicates (N=2, total n>150 for each condition). *P≤0.05, **P≤0.01, ***P≤0.001, ****P≤0.0001.

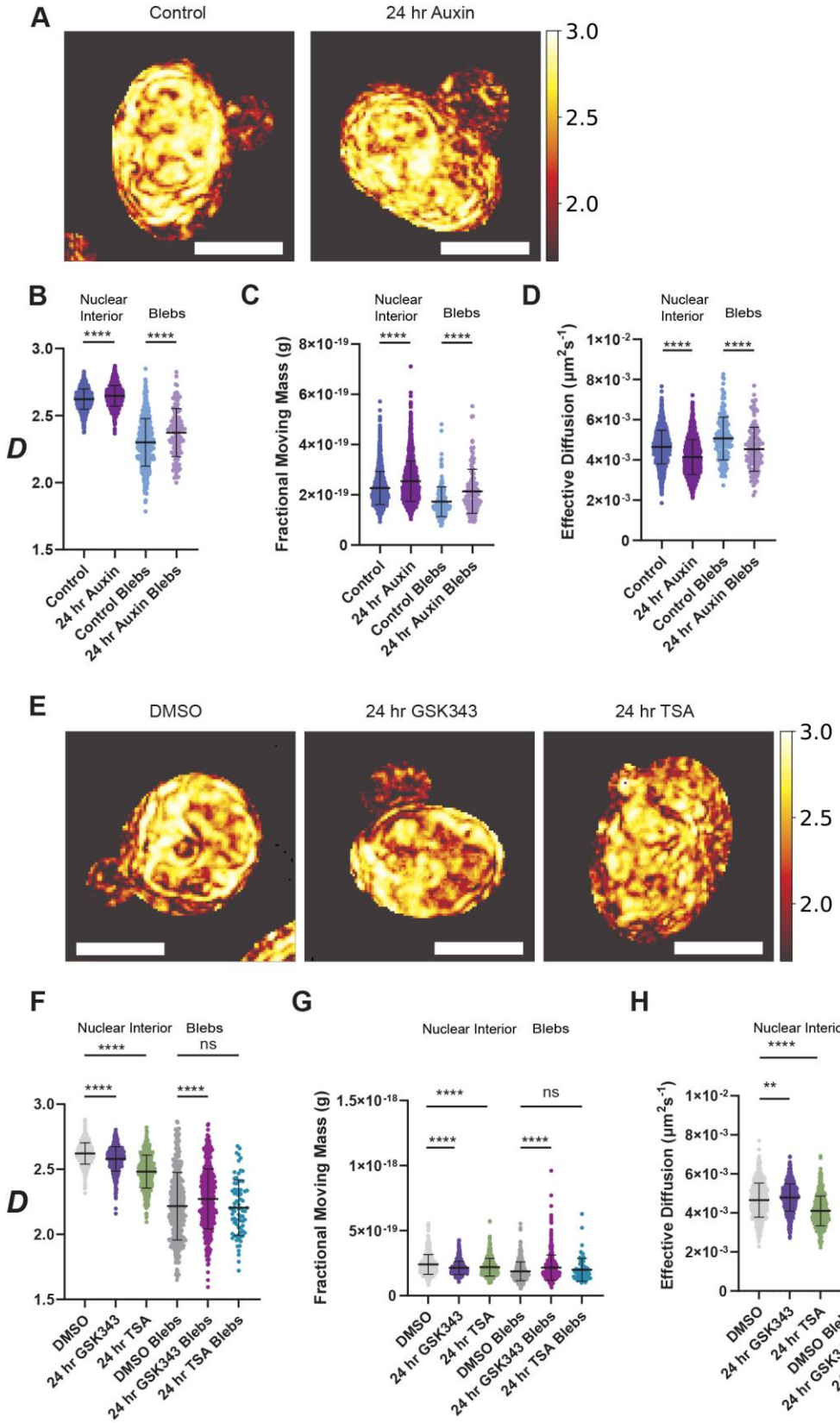

Fig. 2. Loss of B-type lamins, EZH2i, and HDACi induce a bleb-associated chromatin phenotype. (A) Representative PWS *D* maps and (B) *D* values for the nuclear bodies and nuclear blebs for control and 24-h auxin-treatment conditions in HCT116$^{LMN(B1\&B2)\text{-}AID}$ cells. (C) Fractional moving mass values for nuclear bodies and nuclear blebs for control and 24-h auxin-treatment conditions in HCT116$^{LMN(B1\&B2)\text{-}AID}$ cells. (D) Effective diffusion coefficient values for the nuclear bodies and nuclear blebs for control and 24-h auxin-treatment conditions in HCT116$^{LMN(B1\&B2)\text{-}AID}$ cells. (E) Representative PWS *D* maps and (F) values for the nuclear bodies and nuclear blebs for DMSO (vehicle control), 24-h GSK343, and 24-h TSA-treatment conditions in HCT116$^{LMN(B1\&B2)\text{-}AID}$ cells. (G) Fractional moving mass values for the nuclear bodies and nuclear blebs for DMSO (vehicle control, 24-h GSK343, and 24-h TSA-treatment conditions in HCT116$^{LMN(B1\&B2)\text{-}AID}$ cells. (H) Effective diffusion coefficient values for the nuclear bodies and nuclear blebs for DMSO (vehicle control), 24-h GSK343, and 24-h TSA-treatment conditions in HCT116$^{LMN(B1\&B2)\text{-}AID}$ cells. For (B-D, F-H), each dot represents a cell nucleus. (Control n=2451, Auxin n=2140, Control Blebs n=200, Auxin Blebs n=129, DMSO n=741, GSK343 n=790, TSA n=498, DMSO Blebs n=564, GSK343 Blebs n=467, TSA Blebs n=77). Error bars represent mean±s.d. Data are compiled from three technical replicates (N=3). Violin plots show the median and quartiles for the unpaired two-tailed *t*-test between selected groups. *P≤0.05, **P≤0.01, ***P≤0.001, ****P≤0.0001. Scale bars=5 µm.

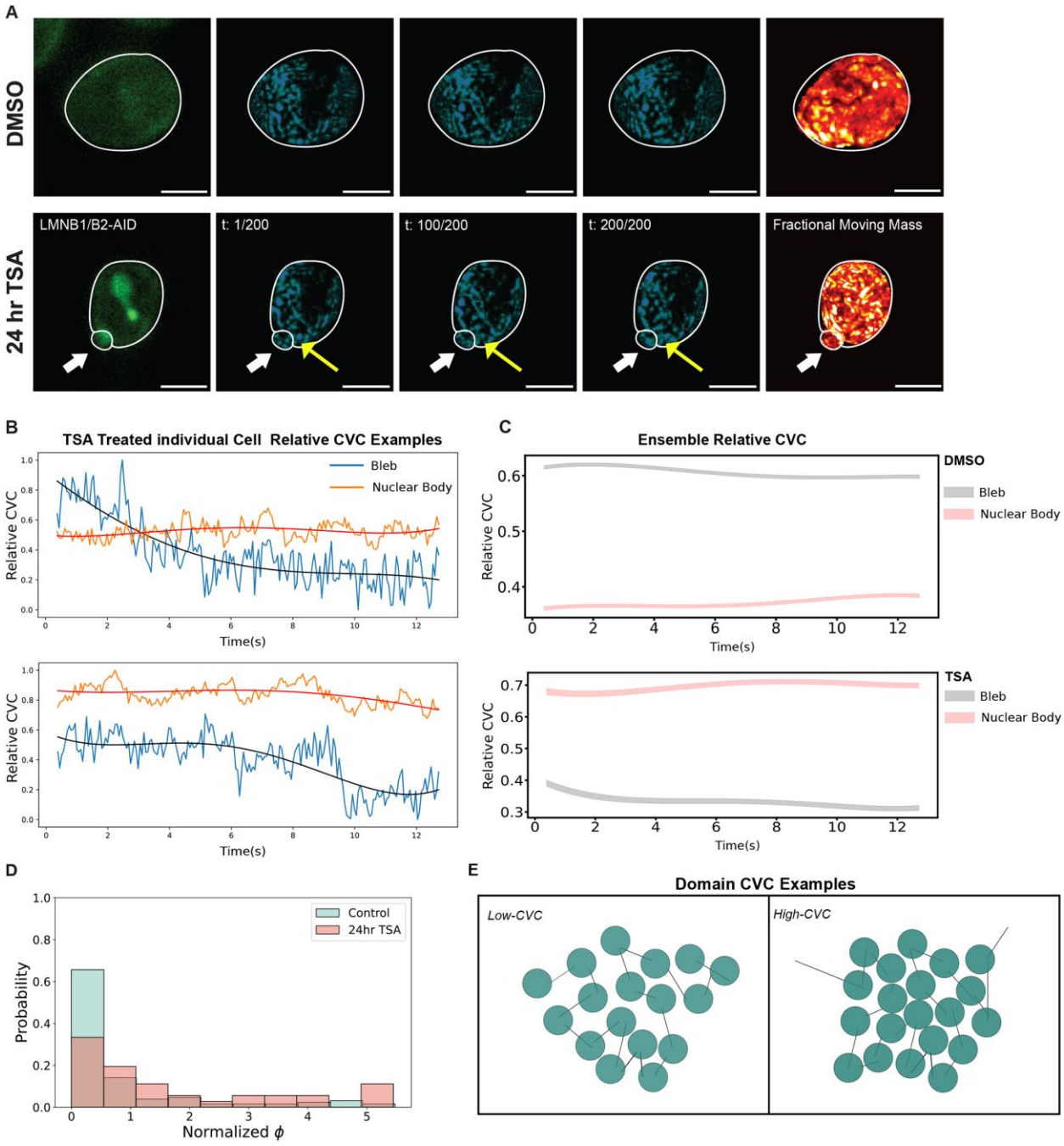

Fig. 3. Chromatin density decreases rapidly in the boundary adjacent to the nuclear bleb. (A) Representativ fluorescent mClover signal images, fractional moving mass "hot" heat map, and individual frames of the temporal interference signal, inversely proportional to chromatin density over the imaging acquisition time of live HCT116$^{LMN(B1\&B2)\text{-}AID}$ cells (non-degraded) for DMSO (control) and 24-h TSA treatment all acquired via the Dual-PWS system. White Arrows

indicate nuclear blebs and yellow arrows indicate areas of interest of motion. Data are representative of three technical replicates (*N*=3; DMSO *n*=741, TSA *n*=498). Fluorescent, fractional moving mass, and individual frame images have the same scaling between treatment conditions. Scale bars=5 μm. (B) Representative Relative CVC change over time for two regions of interest in a single cell treated with TSA within the dataset. Blue and orange curves represent the Relative CVC for blebs and nuclear body respectively. Both colors show the original dynamic PWS intensity as a function of time, with high frequency components measuring the FMM and the low frequency components records the average CVC change. Fourth order polynomial is fit to the raw signal as shown by the red and black curves following the body and bleb signal respectively. (C) Is ensemble relative CVC for all nuclei in DMSO (Top) and TSA (bottom) treated conditions over time. Line and shaded region represent average fourth order polynomial fit with standard error. (D) Bleb average CVC for DMSO (Control: 172 bleb, 308 body) and 24-h TSA treatment (Treated: 40 bleb, 217 body) measured from dynamics PWS signal for nuclear body and bleb regions. Data are the same as of (A). (E) Shows Bleb body ratio for relative CVC measurements for CTRL (98 pairs) and SA (31 pairs) treatment conditions. (F) Schematic illustrating the differences between low and high CVC domains.

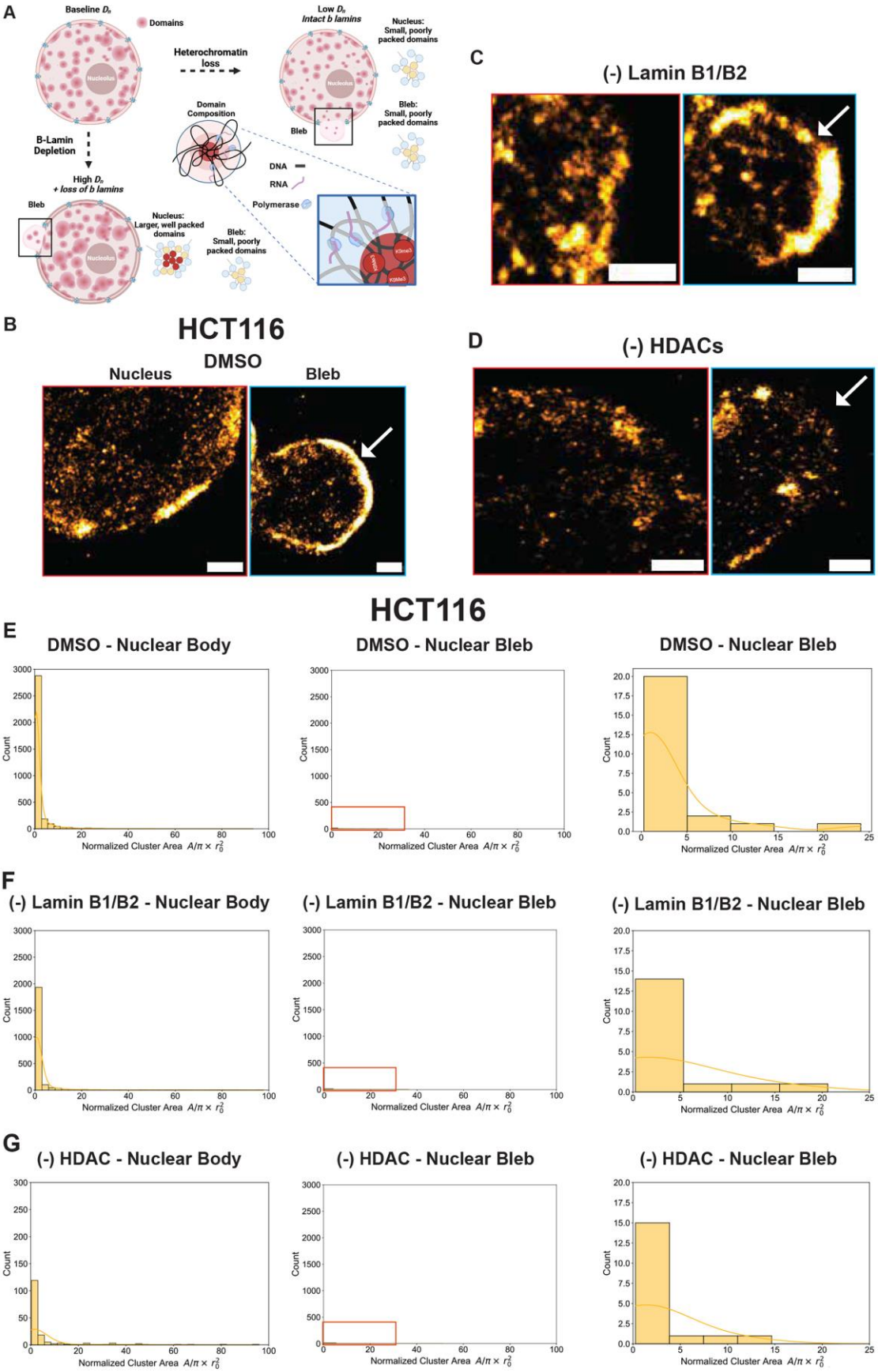

Journal of Experimental Biology • Accepted manuscript

Fig. 4. Characterization of heterochromatin nanodomains from SMLM images in HCT116 cells. (A) Schematic of nucleus illustrating heterochromatin nanodomains. Change in D and inhibition of heterochromatin (HDACi) causes domain collapse and fragmentation in the blebs. While treatment with auxin leads to loss of b type lamin and higher Dn. As highlighted, the nuclear blebs contain small domain cores. (B) Representative SMLM images of HCT116$^{LMN(B1\&B2)\text{-}AID}$ cells with zoomed-in views before (DMSO (300 nM) and after (C) 24-h auxin treatment or (D) 24-h TSA treatment (300 nM). Yellow: H3K9me3. Scale bars=1 µm for inset of whole nucleus (red border) and nuclear bleb (blue border). White arrows placed to highlight presence of H3K9me3 signal in the nuclear blebs. (E-G) Quantification of the number and size of heterochromatin nanodomains in control, auxin and TSA treatment conditions for HCT116 cells within nuclear body and nuclear bleb formation. Data presented in a 3×3 panel, where the first panel is the count for the nuclear body, the middle panel is the nuclear bleb with the same scale used in the and the third panel is the same data, but adjusted scales so the histogram count is visible.

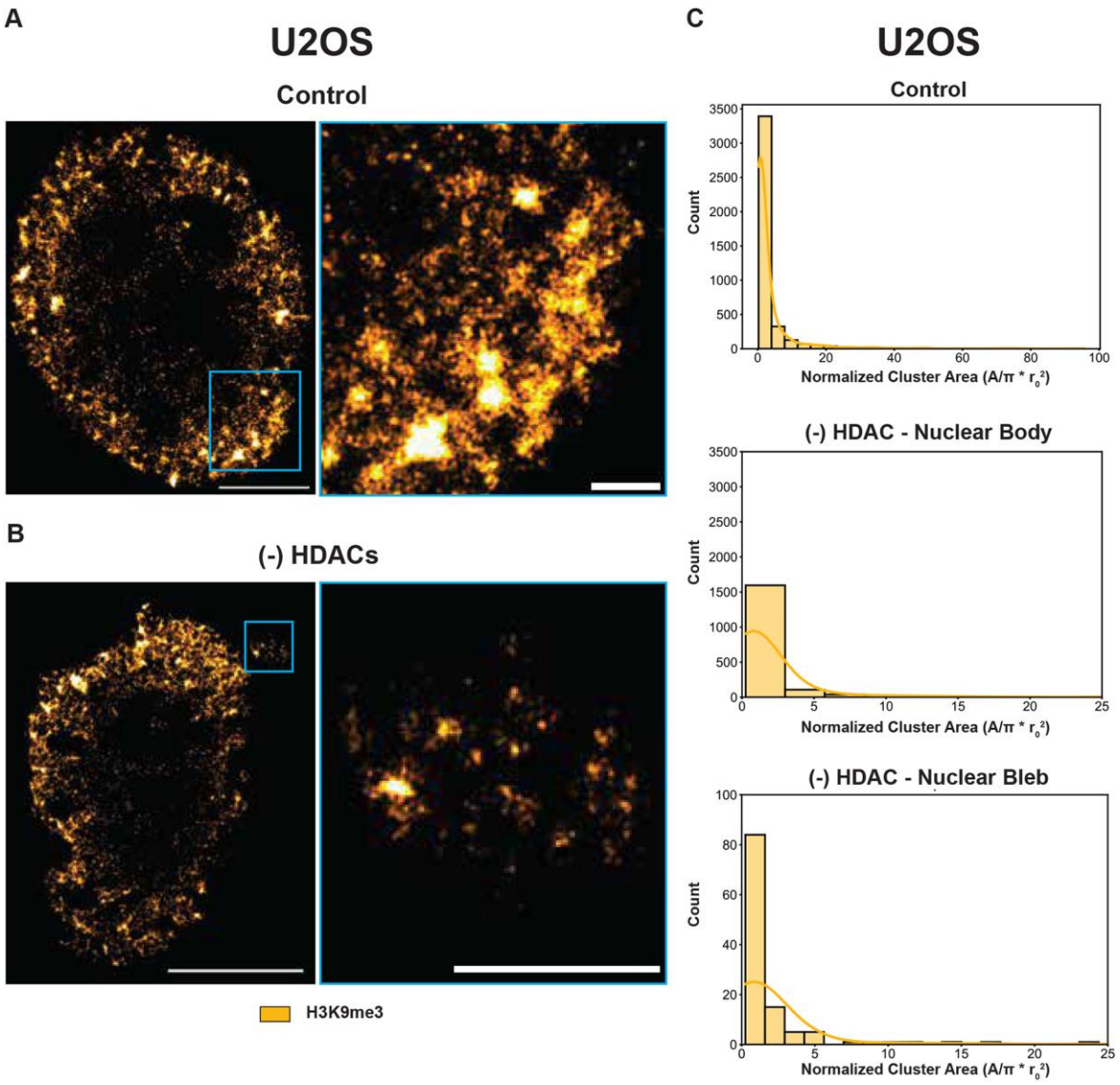

Fig. 5. Heterochromatic nanodomains are reorganized during nuclear bleb formation. (A) Representative SMLM images of U2OS cells with zoomed-in views before and (B) 24-h TSA treatment. Yellow: H3K9me3. Data are representative of three technical replicates (*N*=3; Control *n*=3, TSA (- HDAC) *n*=3). Scale bars=5 µm for whole nucleus, 1 µm for inset of nuclear bleb (blue). (C) Quantification of the number and size of heterochromatin nanodomains in control, and TSA treatment conditions for U2OS cells.

Table 1. Dual-PWS measurements of nuclear blebs

Condition	Average D (Mean±s.e.m.)	Average FMM (g) (Mean±s.e.m.)	Average D_e ($\mu M^2/s$) (Mean±s.e.m.)
Control (Untreated)	2.30	1.76×10^{-19}	5.09×10^{-3}
Control (DMSO)	2.22	1.89×10^{-19}	5.12×10^{-3}
(−) Lamin B1/B2	2.37 (±0.03)	2.26×10^{-19} (±	4.35×10^{-3} (±0.0003)
(−) EZH2	2.27 (±0.03)	2.16×10^{-19} ($\pm1.53\times10^{-20}$)	4.71×10^{-3} (±0.0001)
(−) HDACs	2.20 (±0.03)	1.99×10^{-19} ($\pm1.53\times10^{-20}$)	4.34×10^{-3} (±0.0001)

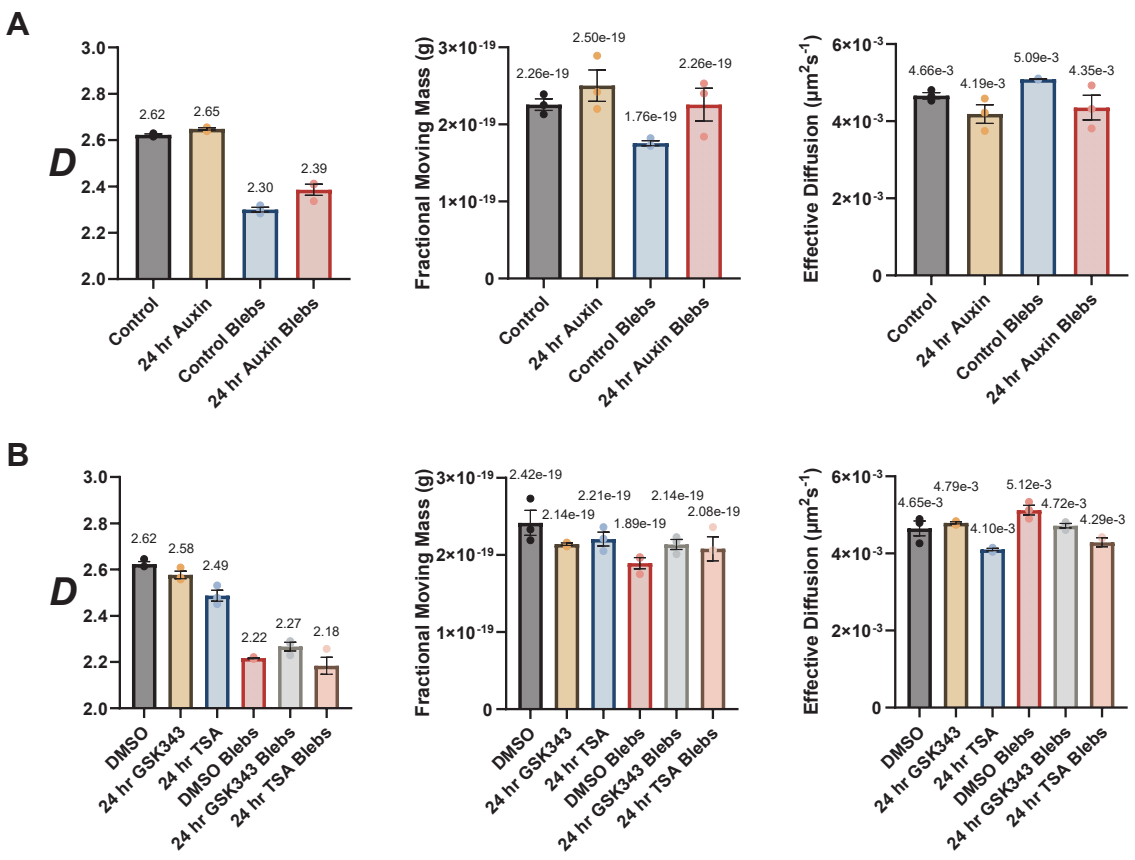

Fig. S1. Nuclear blebbing induces the redistribution and reorganization of packing domains.

(A) Averages of all three replicates for *D* values, fractional moving mass, and effective diffusion coefficient for the nuclear bodies and nuclear blebs for control and 24-hour auxin-treatment conditions in HCT116$^{LMN(B1\&B2)\text{-}AID}$ cells. **(B)** Averages of all three replicates for *D* values, fractional moving mass, and effective diffusion coefficient for DMSO (vehicle control) 24-hour GSK343, and 24-hour TSA-treatment conditions in HCT116$^{LMN(B1\&B2)\text{-}AID}$ cells. For **(A, B)** means of all replicates are presented above each bar in the plots. Error bars represent mean ± SEM. For **(A-B)**, Data are compiled from three technical replicates (N = 3; Control n = 2451, Auxin n = 2140, Control Blebs n = 200, Auxin Blebs n = 129, DMSO n = 741, GSK343 n = 790, TSA n = 498, DMSO Blebs n = 564, GSK343 Blebs n = 467, TSA Blebs n = 77).

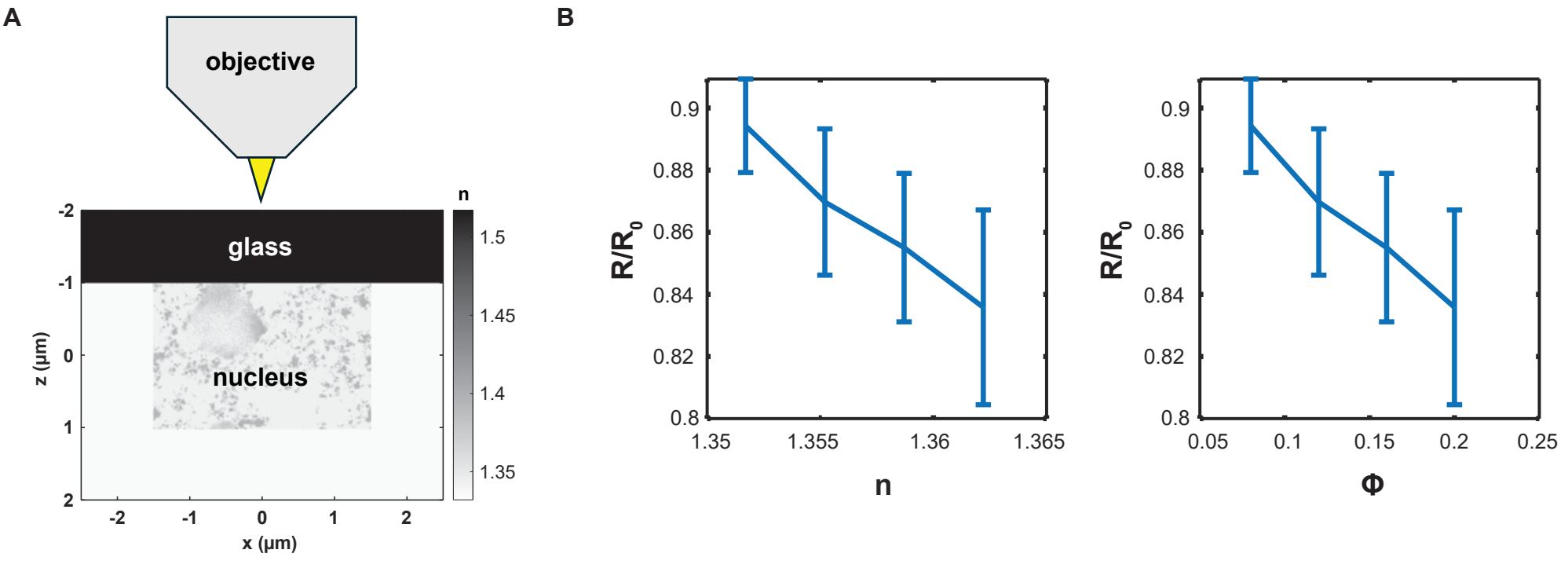

Fig. S2. FDTD simulation confirms the correlation between PWS Intensity with nuclear average RI and CVC.
(A) Schematic of FDTD simulation setup. Light is illuminated from objective and focused on the cell glass interface. Random media with autocorrelation coefficients representing chromatins are placed into the simulation space. By solving Maxwell equations numerically, the back scattering light intensity field is resolved and used to synthesize simulation PWS images. **(B)** Negative correlation between PWS normalized reflectance and media average RI and phi. n = 10 for each condition.

Table S1. Average Number of Nuclei, Blebs and Micronuclei per FOV across three replicates

	Control	DMSO	24 hr. Auxin	24 hr. GSK343	24 hr. Auxin + GSK 343	24 hr. TSA	24 hr. Auxin + TSA
# of Nucelli	379.50	98.33	388.50	365.33	311.00	152.00	152.00
# Blebs	7.00	1.33	21.00	24.33	25.33	26.33	37.33
# Micro-nuclei	3	0.667	18.5	9.333	9.667	12.000	13.000

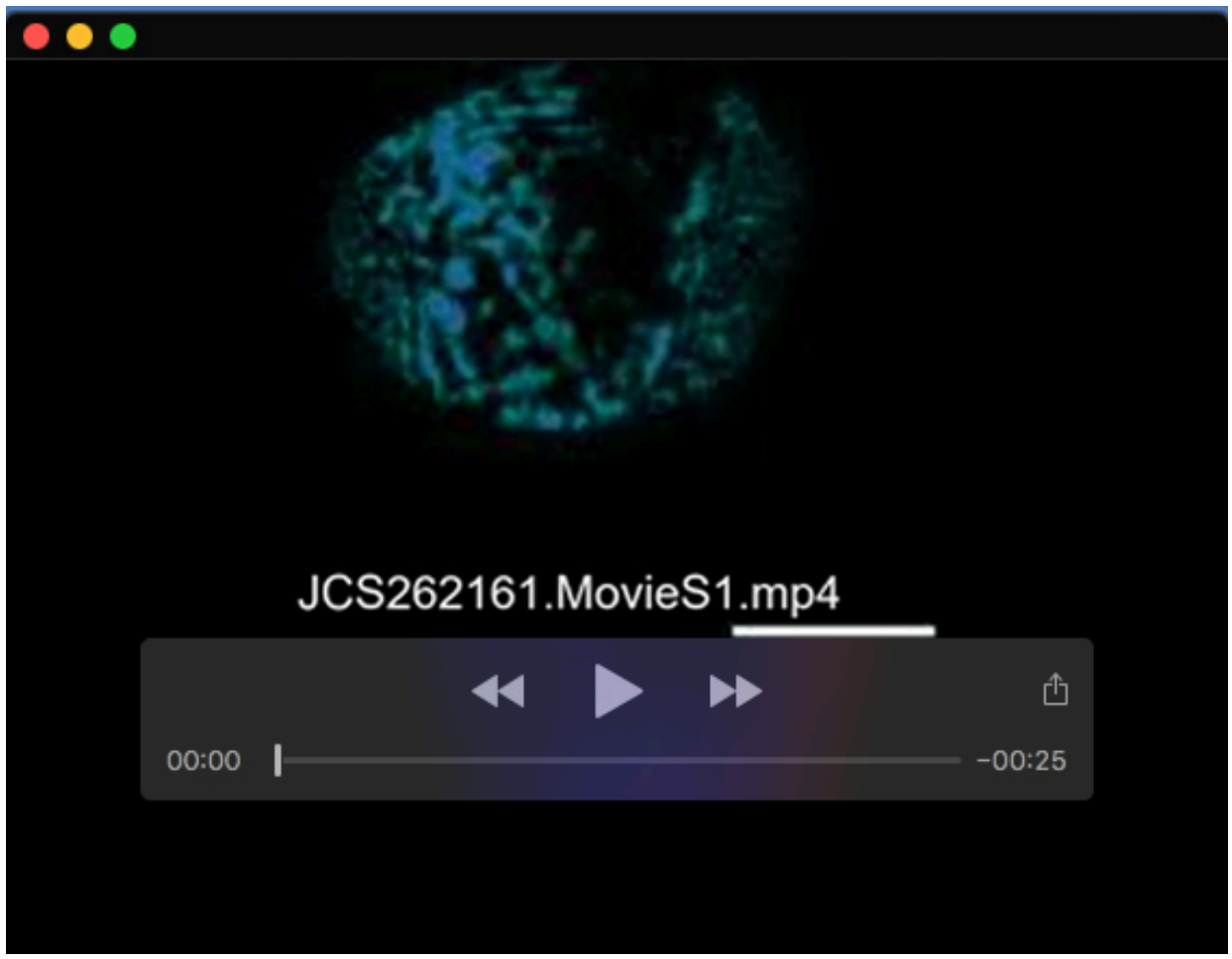

Movie 1. Fractional Moving Mass and Representative CVC time series Movies. Time series Fractional moving mass for HCT116 cell treated with DMSO corresponding to Fig. 3A Top.

Movie 2. Fractional Moving Mass and Representative CVC time series Movies. Time series Fractional moving mass for HCT116 cell treated with TSA corresponding to Fig.3A Bottom.

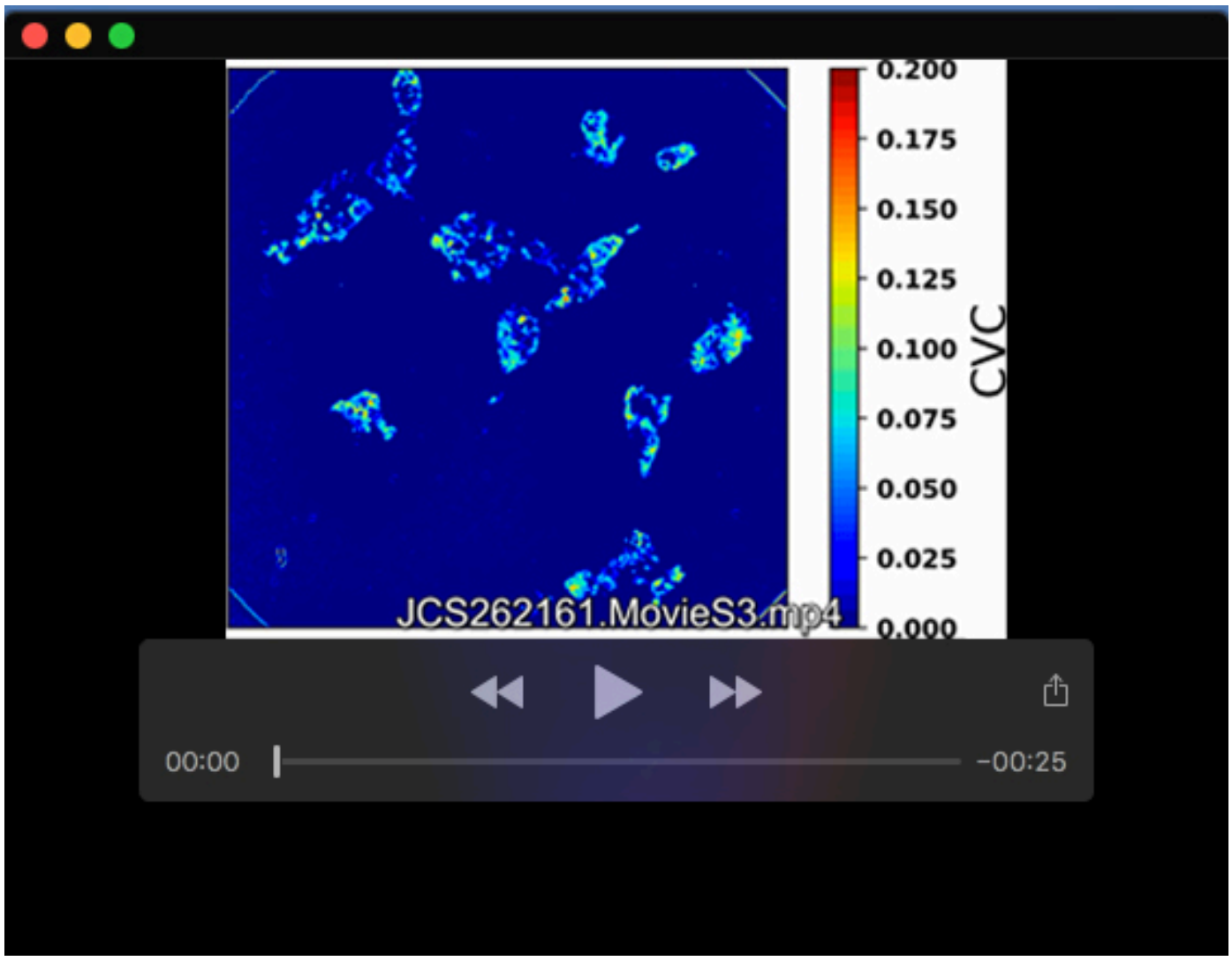

Movie 3. Fractional Moving Mass and Representative CVC time series Movies.
Representative imaging of CVC time series for full field of view of HCT116 Cells.